

# Design of an Electric Propulsion System for SCEPTOR

Arthur Dubois\* , Martin van der Geest † and JoeBen Bevirt ‡*Joby Aviation, Santa Cruz, CA, 95060, USA*

Sean Clarke§

*NASA Armstrong Flight Research Center, Edwards, CA, 93523, USA*

Robert J. Christie¶

*NASA Glenn Research Center, Cleveland, OH, 44135, USA*

Nicholas K. Borer||

*NASA Langley Research Center, Hampton, VA, 23681, USA*

The rise of electric propulsion systems has pushed aircraft designers towards new and potentially transformative concepts. As part of this effort, NASA is leading the SCEPTOR program which aims at designing a fully electric distributed propulsion general aviation aircraft. This article highlights critical aspects of the design of SCEPTOR's propulsion system conceived at Joby Aviation in partnership with NASA, including motor electromagnetic design and optimization as well as cooling system integration. The motor is designed with a finite element based multi-objective optimization approach. This provides insight into important design trade-offs such as mass versus efficiency, and enables a detailed quantitative comparison between different motor topologies. Secondly, a complete design and Computational Fluid Dynamics analysis of the air breathing cooling system is presented. The cooling system is fully integrated into the nacelle, contains little to no moving parts and only incurs a small drag penalty. Several concepts are considered and compared over a range of operating conditions. The study presents trade-offs between various parameters such as cooling efficiency, drag, mechanical simplicity and robustness.

## Nomenclature

|                 |                                   |
|-----------------|-----------------------------------|
| $D$             | Nacelle Drag                      |
| $D_{clean}$     | Clean Nacelle Drag                |
| $D_{cooling}$   | Cooling Drag                      |
| $\mathcal{T}$   | Torque on the Nacelle             |
| $\dot{E}_{tot}$ | Total Power Supplied to the Motor |
| $v$             | Aircraft Speed                    |

## I. Introduction

With recent advances in battery technology, electric propulsion systems are growing increasingly popular amongst general aviation aircraft. As part of this dynamic, NASA is leading the Scalable Convergent Electric Propulsion Technology Operations Research (SCEPTOR) program which aims at designing, building and testing a demonstrator aircraft to showcase distributed electric propulsion technology. Benefits of such technology include lower emissions, reduced energy consumption and smaller noise signature. SCEPTOR's propulsion system is to be composed of 12 smaller high lift propellers distributed along the span of the wing to be used during take-off and landing as well as two

\*Aeronautical Engineer, 340 Woodpecker Ridge, Santa Cruz, CA, 95060, USA, AIAA Member.

†Brushless Motor Design Engineer, 340 Woodpecker Ridge, Santa Cruz, CA, 95060, USA.

‡Founder, 340 Woodpecker Ridge, Santa Cruz, CA, 95060, USA.

§SCEPTOR co-Principal Investigator, Advanced Systems Development Branch, PO Box 273/MS4840D.

¶Aerospace Engineer, Thermal Systems Branch, 21000 Brookpark Rd, MS 86/12.

||Technical Lead/Aerospace Engineer, Aeronautics Systems Analysis Branch, MS 442, AIAA Senior Member.

bigger cruise propellers placed at the wingtips as shown in figure 1. Tip propellers are the sole source of propulsion during climb and cruise while distributed propellers are used during take-off and landing to blow the wing and increase dynamic pressure. In an effort to minimize drag, frontal area of the tip propellers must be maintained to a minimum. The resulting tip motor features high power density which poses significant challenges from an electromagnetic and cooling standpoint. This paper outlines the design process for SCEPTOR's tip nacelle, including motor and cooling system. Section II introduces some background information about the program and presents several design trade-offs. Section III focuses on the electromagnetic design of the motor while section IV outlines the design of the cooling system. The resulting propulsion system is then analyzed in details in section V. Finally, the paper is concluded in section VI.

## II. Background

### A. Distributed Electric Propulsion

Electric propulsion technology is quickly and significantly impacting aircraft design. Electric motors, thanks to their simplicity, reliability and scalability can not only be used to replace combustion engines, but also open the door to completely new wing configurations. One example of such configurations is the Distributed Electric Propulsion (DEP) system which leverages the small size and scalability of electric motors to blow the wing using a multitude of small propellers strategically placed along the span.<sup>1</sup> DEP systems alleviate the need for traditional high-lift devices by increasing the dynamic pressure over the wing to improve the stall performance of the aircraft. This not only reduces mechanical complexity, but also allow the design to be tuned such that the wing can operate in near-optimal conditions during cruise, hence significantly reducing drag. On the other hand, combustion engines are too complex to be scaled down and, unlike electric motors, see significant decrease in specific power once their size is reduced. As a result, their use in distributed propulsion is not as easily implemented and aircraft featuring combustion engines must rely on high-lift devices at low speed which renders their wing design sub-optimal in cruise. DEP also provides advantages in terms of redundancy, low-speed propeller design, interference drag reduction and controls. NASA has been demonstrating the use of DEP through the LEAPTech program since 2014 and tests are ongoing<sup>2</sup> via a test platform mounted on a truck as shown in figure 2.



Figure 1: SCEPTOR Design.



Figure 2: LEAPTech Distributed Electric Propulsion Testbed.

### B. SCEPTOR Program

The SCEPTOR program is the continuation of the LEAPTech project and focuses on designing and building a demonstrator aircraft for DEP technology validation. The aircraft is based on a Tecnam P2006T fuselage fitted with a DEP wing. The propulsion system is composed of two cruise propellers located on the wing tips and 12 smaller propellers distributed along the span for low speed operations. The 12 small propellers are used during take-off and landing to blow the wing in order to increase dynamic pressure on the wing so as to decrease the stall speed. During cruise operations, the high lift propellers are turned off and the cruise propellers provide all of the necessary thrust. Since wings are optimized solely for cruise operations, the drag on the airplane is reduced as compared to the stock Tecnam 2006T aircraft.

### C. Cruise Propulsion System

The remaining of this paper will focus on the design of the motors and cooling system of SCEPTOR's cruise propulsion systems. Each tip nacelle is to be composed of a single electric motor providing up to 66 and 85kW of continuous and peak power respectively, along with an appropriately sized air cooling system. The cooling system must in addition be able to cool the motor inverters, although that last point will not be discussed in this paper. Due to aerodynamic considerations, the frontal area of the nacelle must be maintained as small as possible. Hence, the system features a high power density and relatively little room for cooling. Moreover, unlike airplane combustion engines which routinely run at several hundred degrees, electric motors components have more stringent temperature requirements. Another critical parameter to be considered is motor efficiency as it is tightly correlated with cooling, and great simplifications in the cooling system can be achieved by increasing motor efficiency. However, an inadequate estimate of motor efficiency could result in undersized cooling system components leading to overheating and eventually failure of the motor. Hence, accurate simulation and testing must be performed in order to converge to a good overall solution, both from motor design and system cooling perspective. In this paper, motor design is obtained via multi-objective optimization using Finite Element Analysis to estimate the performance. On the other hand, the cooling system is analyzed using Computational Fluid Analysis coupled with a Heat Transfer solver. The simulations are carried out via STARCCM+ © version 10.04 using a steady RANS solver and a  $k - \epsilon$  turbulence model.

Broadly speaking, there are two families of cooling systems: liquid cooled and air cooled. Liquid cooling systems typically provide better performance but tend to increase the mechanical complexity of the system due to the necessity of adding auxiliary pumps, tubing and heat exchanger for the fluid. They also provide much better static cooling performances than air cooled systems which tend to severely under-perform in the absence of air flow. On the other hand, air cooled motors are mechanically much simpler and hence have a lesser impact on the weight budget. In the spirit of maintaining design simplicity and after a few initial studies, it was decided to opt for an air cooled system.

### D. Operating Conditions

Table 7 shows different operating conditions for the aircraft. The plane is to be designed to operate at up to 8000ft at 150knots in cruise. The motor is expected to supply 60kW of continuous power at 2250rpm during climb. Assuming a motor efficiency of 95%, this means that about 3kW of heat is to be dissipated by the cooling system. Moreover, different conditions must be taken into account. In particular, the cooling system is designed so that the aircraft can operate in hot weather conditions. On top of that, extra safety factors are added to account for factors such as model uncertainty and NASA acceptance margin. The resulting temperature operating conditions are shown in figure 3. The prototype qualification temperature is set to 60°C at sea level which corresponds to about 35°C above typical operating conditions.

Throughout the design selection process, a single temperature operating conditions of 35°C has been utilized in an effort to limit the simulation effort. Hence, all climb cases presented in section IV use this value as the free stream temperature. 35°C represents the upper bound of the envelope where the aircraft is expected to operate. Section V focuses on the selected design and includes a more thorough analysis of its behavior at various temperature conditions, up to prototype qualification temperature.

From a cooling standpoint, the climb phase at low altitude is by far the most critical as free stream temperature is generally higher than in cruise, aircraft speed is reduced and the motors operate at maximum power. Hence, the cooling system must be sized according to these conditions. However, it is also important to consider the impact of the cooling on the total drag of the aircraft during the cruise phase. These considerations will be further detailed in section IV.

Since cooling is heavily influenced by motor efficiency, it is natural to start the design process with the motor design phase so as to get a handle of the performances of various designs before considering cooling.

Table 1: Flight Operating Conditions

| Condition | Speed [KTAS] | Alt [ft]         | Power per Motor [kW] |
|-----------|--------------|------------------|----------------------|
| Cruise    | 150          | 8000             | 43                   |
| Climb     | 110          | Sea Level-8000ft | 60                   |

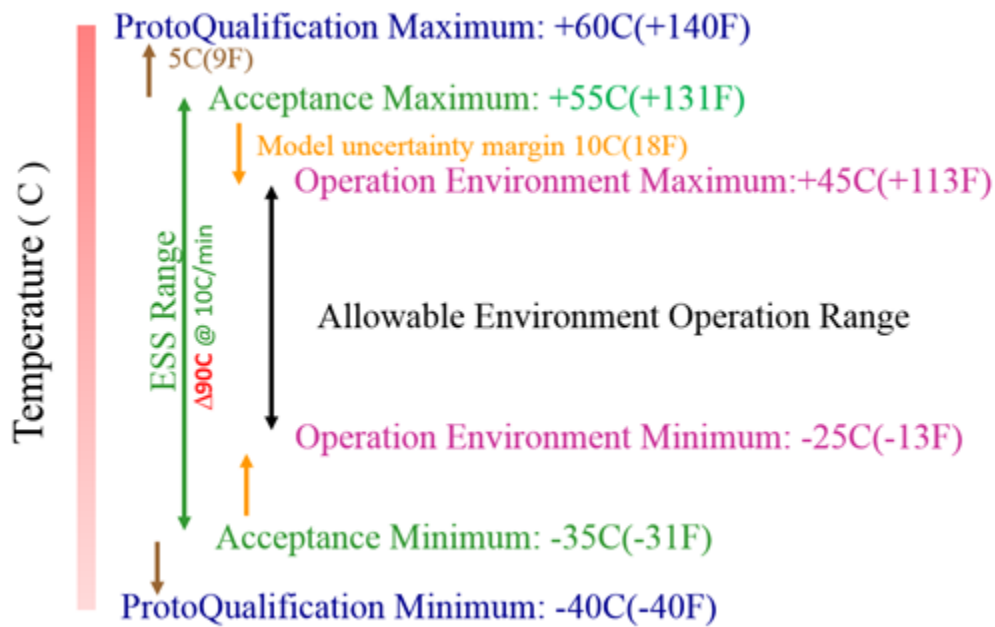


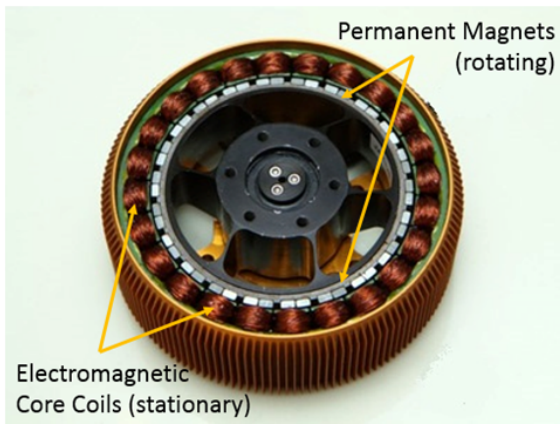
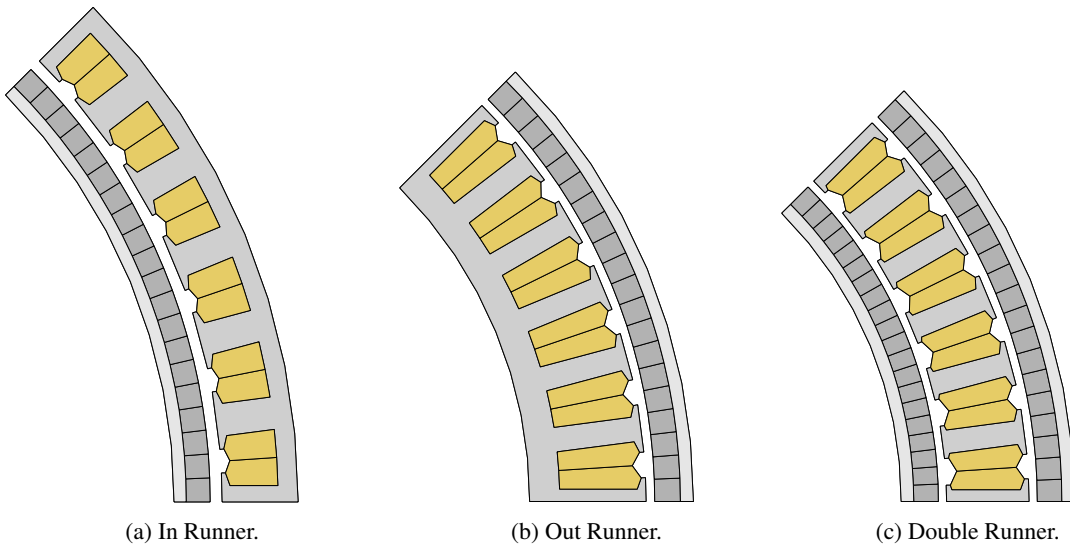
Figure 3: Temperature Operating Conditions.

### III. Motor Design

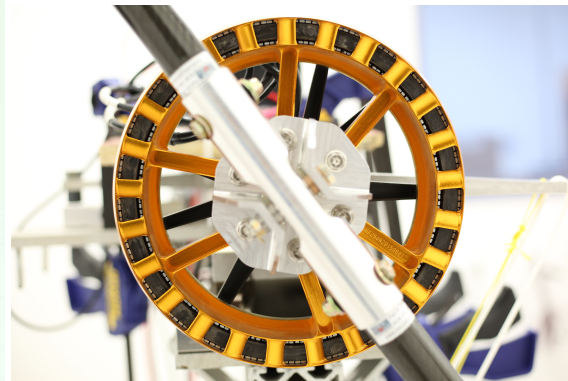
The electromagnetic motor design process consists of selecting a suitable motor type and topology, and sizing the motor parts to obtain satisfactory performance. For this application, only surface mounted permanent magnet synchronous motors (SPM) are considered. PM motors have a higher specific power density than *e.g.* asynchronous motors or switched reluctance motors, because the magnets offer a nearly lossless excitation. Compared to interior (or buried) PM motors, SPMs allow for a higher peak output torque, but have a narrower useful torque-speed operating range,<sup>3</sup> which matches well with the application. From a mechanical or constructional perspective, there is no decidedly better topology; SPM rotors may consist of a simple turned cylindrical shell with magnets glued on, but require a magnet retention sleeve at higher speeds, while IPM rotors require lamination cutting and have reduced magnetic performance at higher speeds, due to the need for thicker rotor parts.<sup>4</sup>

Safety is a particular concern with any PM motor, because the magnets cannot be disabled. If a short circuit occurs –internal or external to the motor– and the rotor is rotating, a current will flow. Short circuits external to the motor can be mitigated with *e.g.* fuses or contactors. Internal short circuits, for instance between turns or coils, cannot be mitigated so easily and are not specifically handled in the current design, as they are statistically uncommon. Techniques to mitigate such faults do exist if needed, but those affect the power density and increase the required inverter size.<sup>5</sup> Inverter failures are on the other hand far more common, so to increase the reliability the winding of each motor will be divided into two equal and electrically separated sets, each driven by an independent inverter. These inverters may then be powered from independent sources for a further increase in reliability.

Many motor topologies exist in terms of flux direction and rotor/stator orientation. For this application, only radial flux motors will be considered, as these offer a proven power density and relatively straight forward construction. Three topologies will be compared: in-runner (IR), out-runner (OR) and double rotor (DR) motors. Figure 4 abstractly shows these topologies. In the DR topology, the stator yoke is replaced by an extra rotor ring with magnets and (necessarily) a second airgap. This eliminates the losses in the yoke, although eddy current losses in the magnets and supporting material can occur instead. An additional benefit of this topology is a reduction in current induced stator saturation, because the double airgap doubles the magnetic reluctance, although this effect may be small when the PM flux alone (nearly) saturates the stator. A disadvantage of the DR topology is the mounting of the individual teeth; a completely potted stator would have to be used, with obvious thermal drawbacks in an air cooled motor. Between these three topologies, the difference in magnetic performance may be small given the diameter of the motor.



(d) Example of In Runner Design.



(e) Example of Double Runner Design.

Figure 4: Motor topologies

## A. High level design and optimization

Multi-objective optimization is used as a first step to explore the design space and globally compare the three motor topologies. The main goal is to identify a realistic target design space and preselect a suitable winding layout.

### 1. Modeling approach

Two dimensional finite element analysis is used to model the magnetic motor performance. The following properties are calculated for each motor in the nominal and boosting operating conditions: the linked PM flux ('back-emf'); synchronous inductance; required phase current and number of turns; loaded torque and torque ripple; iron, copper and rotor losses; and a temperature estimate with a lumped-element network for comparative purposes. Non-linear lamination properties are used where needed. This data provides a complete overview of the expected electromagnetic performance. The models and saturation data used here have been verified on other projects.

### 2. Optimization setup

Three different base winding schemes will be considered, all using tooth coil windings:

- **12 slots / 10 poles:** 36/30, 48/40 and 60/50. This winding scheme offers a good balance between winding factor (0.933) and space-harmonic content.
- **3 slots / 2 poles:** variable pole count from 20 to 50. Compared to the 12/10 winding scheme, this layout typically induces lower rotor eddy-current losses and has a greater number of symmetries for a given slot count, which reduces internal mechanical stresses. It does however have a relatively low winding factor of 0.866, making this winding a poorer choice in lower speed motors.
- **9 slots / 8 poles:** 36/32, 45/40, 54/48. This winding layout has a winding factor slightly higher than the 12/10 layout (0.945), but is more prone to rotor eddy current losses. It is also acoustically noisier than the other winding scheme, because it is the least balanced.

Far more winding schemes exist within the considered slot/pole range, many with a slot/pole ratio close to unity, such as 48/46. Compared to the winding schemes considered here, such windings offer a slightly higher winding factor and a reduced torque ripple, but have fewer mechanical symmetries. This creates lower order internal stresses that need to be handled (bear in mind that the magnetic radial attractive forces between rotor and stator are often larger than the tangential torque producing forces). For example, in the mentioned 48/46 combination the lowest radial force harmonic is a two pole field, while with a 48/40 winding this is an eight pole field. In both cases this harmonic does not produce any torque; it is solely an attraction force between rotor and stator.

For all motors, a halfbach magnet configuration with 4 magnet pieces per pole and aluminum back is considered. The stator stack is build from individual teeth to enable a high copper fill factor to be reached and efficient material usage. Table 3 summarizes the relevant magnetic input properties. Proximity losses in the windings are not included in the optimization, because those can be managed by suitable winding techniques if necessary.

A version of multi-objective particle swarm optimization (PSO) is used. PSO is a gradient free evolutionary algorithm, well suited to finding approximate global optima. For each slot/pole combination and topology 2500 motor designs are analyzed. The variables are relevant dimensions, including the airgap length(s), slot height, tooth width and magnet thickness, see Table 4. These variables are constrained to obtain geometrically feasible designs. No further constraints are used on output variables such as flux or current density. Instead, designs with excessive losses will be suboptimal and are automatically excluded from the Pareto optimal front.

The Pareto objectives are:

- minimize mass,
- maximize efficiency,
- minimize estimated temperature.

## B. Optimization results

The optimization strategy produces a large amount of data. Besides the direct Pareto front, all underlying properties, such as e.g. the loss distribution, key magnetic flux densities, saturation effects, and emf and torque quality indicators are stored, allowing both high and low level trends to be identified. This section will briefly discuss the most essential

Table 2: Key specifications

| Requirement     | Target                         |
|-----------------|--------------------------------|
| System mass     | 35 kg                          |
| Speed           | 2250 RPM nominal, 2700 RPM max |
| Torque          | 300 Nm nominal, 400 Nm max     |
| Battery voltage | 400–525 V                      |

Table 3: Electromagnetic input properties

| Aspect      | Value                              |
|-------------|------------------------------------|
| Laminations | 0.1 mm high silicon content        |
| Magnets     | NdFeB, grade 45SH<br>Halbach array |
| Fill factor | 50%                                |
| Rotor yokes | Aluminum                           |

Table 4: Optimization variables and range(mm)

| Variable              | Minimum | Maximum |
|-----------------------|---------|---------|
| Stack length          | 50      | 160     |
| Outer active diameter | 200     | 350     |
| Magnet thickness      | 4       | 15      |
| Airgap length         | 2       | 4       |
| Stator yoke thickness | 3       | 15      |
| Slot height           | 12      |         |
| Tooth width           | 33%     | 80%     |
| Tooth tip width       | 25%     | 85%     |

results. First, the Pareto optimal fronts and related scatter plots will be discussed, giving a very high level overview. Thereafter the Pareto fronts are filtered for a numerical overview.

### 1. Pareto fronts

Figure 5 shows a side-view to the Pareto optimal front, demonstrating the basic trend that a heavier motor typically has a higher efficiency. It also shows that from an efficiency perspective and when neglecting all other performance aspects, 12–15 kg is probably the minimum acceptable motor mass, and that the maximum achievable efficiency is about 97.2%. To compare the various winding schemes, the limits of the Pareto optimal fronts are indicated in figure 6. This reveals that the DR motors potentially have the highest efficiency, up to 0.3% above the best IR motors which in turn perform 0.1–0.2% better than the best OR motors. The 30 and 32 pole motors generally perform poorly, except at very high masses where the lower electrical frequency limits the iron losses. The differences between the remaining combinations and topologies are generally so small that the efficiency should not be the leading factor when selecting a certain topology.

Figure 7 shows the outer dimensions. The DR motors are generally the shortest motors for a given mass while the OR motors are the longest, which follows naturally from their shapes and constraints. The outermost radius for all motors tends towards to the maximum value of 175 mm, suggesting that some topologies could magnetically benefit from a further increased radius. Figure 8 shows the magnetic airgap length. A shorter airgap appears to be better, although this is not a hard requirement; 2.5 mm could still work well, or even more for the lower pole count motors.

Figs. 9 and 10 show the copper losses and current density. The latter is a very rough indication of the thermal feasibility of a motor given a certain cooling approach. For a larger air-cooled motor, values above 10 A/mm<sup>2</sup> tend to become problematic, suggesting a mass of 20 kg is more realistic. No major differences exist between the winding layouts considered, except higher values on the low pole count and 3/2 winding family motors.

Figure 11 shows a few simple to explain trends in the iron losses. Heavier motors will have more iron mass, all subjected to a magnetic field, so will have more iron losses; and higher pole count motors have a higher electrical frequency, which induces more losses.

Figure 12 shows the rotor losses, which span almost an order of magnitude between the considered motor configurations. Motors with the 3/2 winding layout perform well, which was one reason to include them, while the 36/32 motors perform particularly poorly. The DR motors are no worse than the other motors, despite having two rotors, because the armature field experienced by each rotor side is halved compared to an IR or OR motor.

Figure 13 shows the temperatures estimated with a lumped element thermal model. This model was used to select cooler motors during optimization. The double rotors perform best, but this may be the result of overestimating the

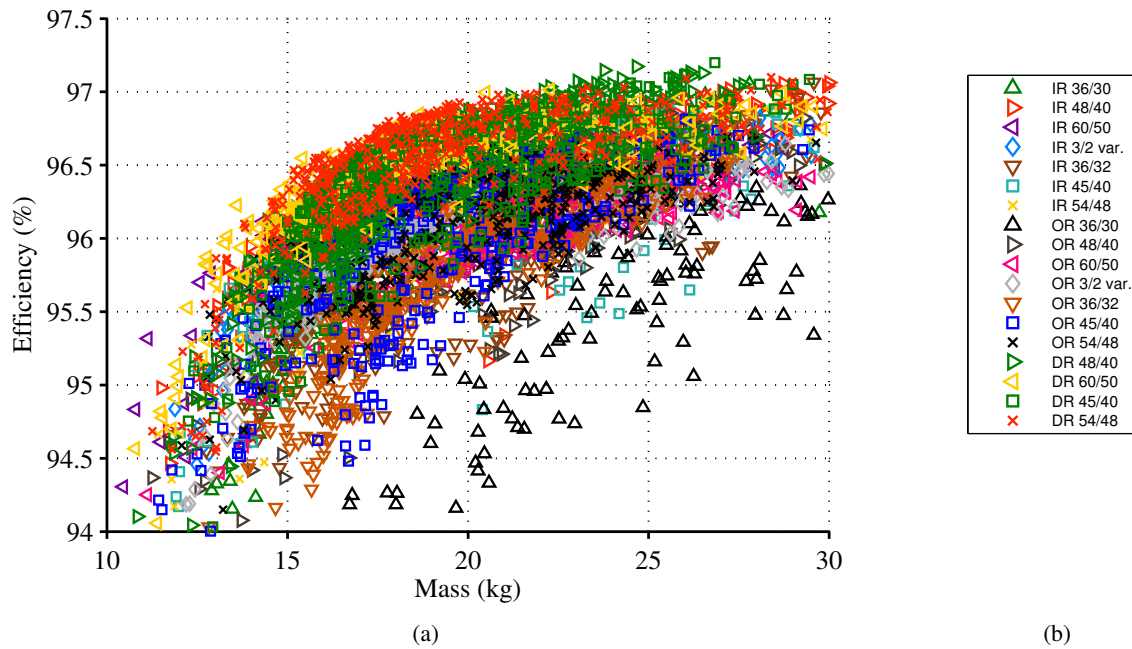


Figure 5: a) 2D sideview to Pareto optimal front: efficiency under nominal conditions versus mass. b): marker definition

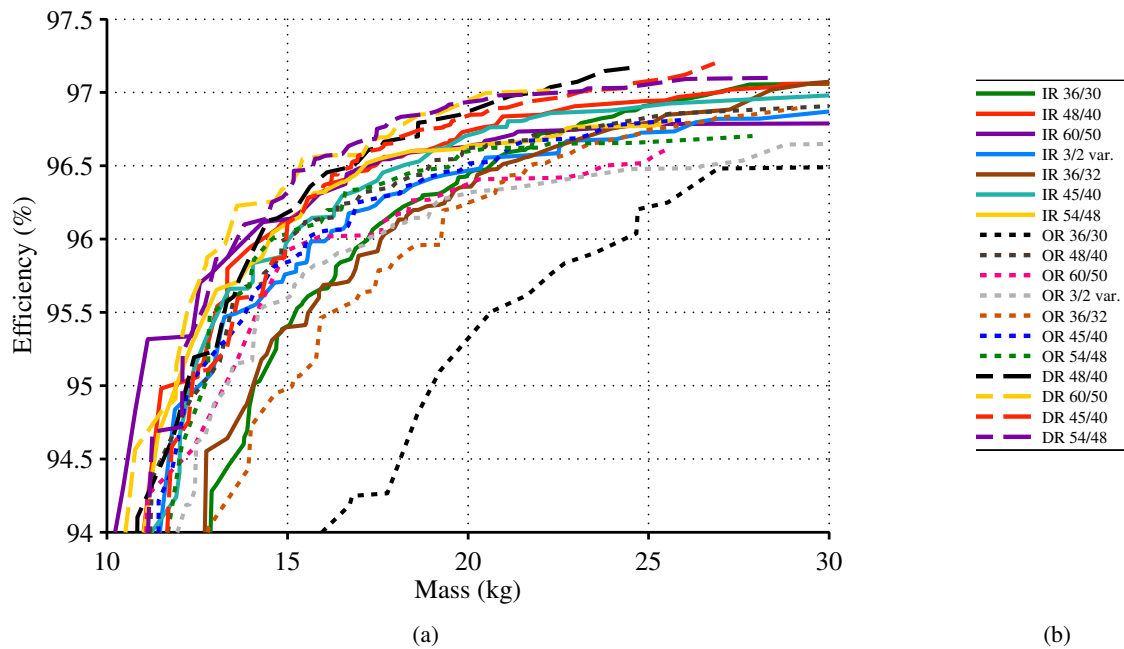


Figure 6: a) Outer limits of the Pareto optimal front. b) line definition; IR=inner rotor, OR=outer rotor, DR=double rotor

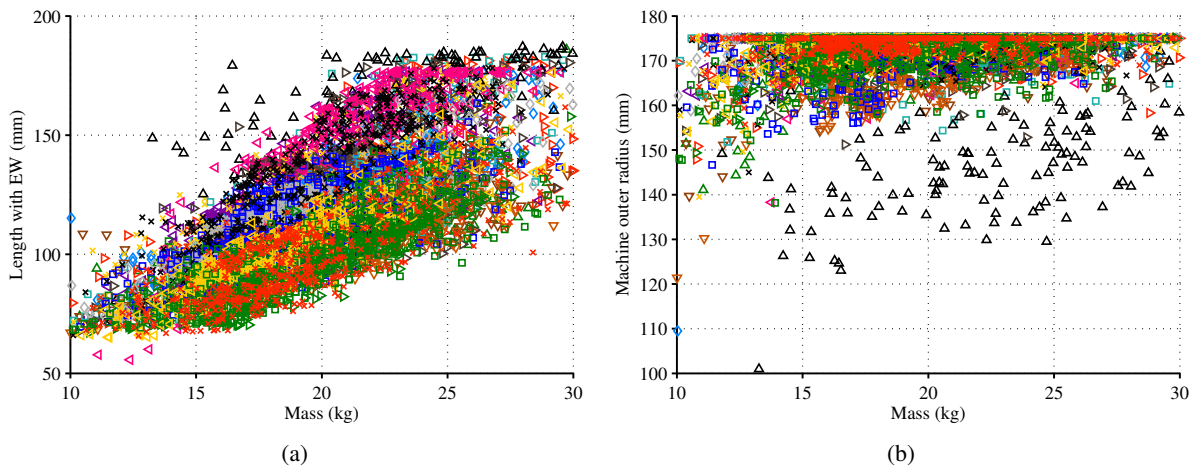


Figure 7: Outer dimensions of the motors: a) length b) outer radius

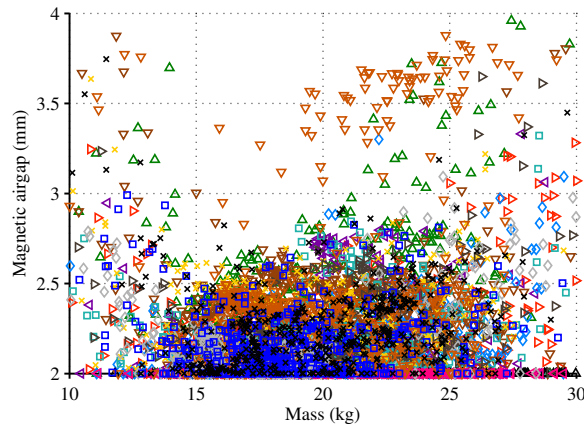


Figure 8: Magnetic airgap length

potting conductivity. If a 100°C winding temperature is acceptable, the lightest DR motor weighs 17 kg, the lightest IR 21 kg and the lightest OR 21.5 kg.

Figure 14 shows the inductance in per-unit values referred to the nominal operating point. The per-unit inductance is more relevant than the absolute inductance from a high level dimensioning perspective, because the former provides a direct indication of the expected power factor and so the minimum inverter size, regardless of the pole-count and magnet flux level. Excessively high inductances will worsen the power factor, limiting the peak output power and increasing the required inverter VA-rating. Too low values on the other hand will limit the possibilities of using flux weakening to reach higher speeds and will increase the current ripple for a given inverter switching frequency, which increases parasitic losses in the motor. Increasing the switching frequency can solve this, but shifts the losses to the inverter. For the more realistic motors the values are around 0.12 pu to 0.4 pu, which can be considered low to good values. The DR motors occupy the lower end of the range, because the double airgap approximately halves the inductance when keeping everything else the same.

## 2. Pareto front filtering

Each of the Pareto fronts in the previous section shows the limits in two variables at once, but relating more than two figures simultaneously is almost impossible. This is important though, as a design with e.g. a very high efficiency not necessarily performs well in other areas. The Pareto fronts are therefore filtered with the criteria summarized in Table 5. Filters 1, 2 and 7 are straight forward. Filter 3 is included to account for the demagnetization risk of the magnets. Filters 4, 5 and 6 prevent heavy saturation of the iron.

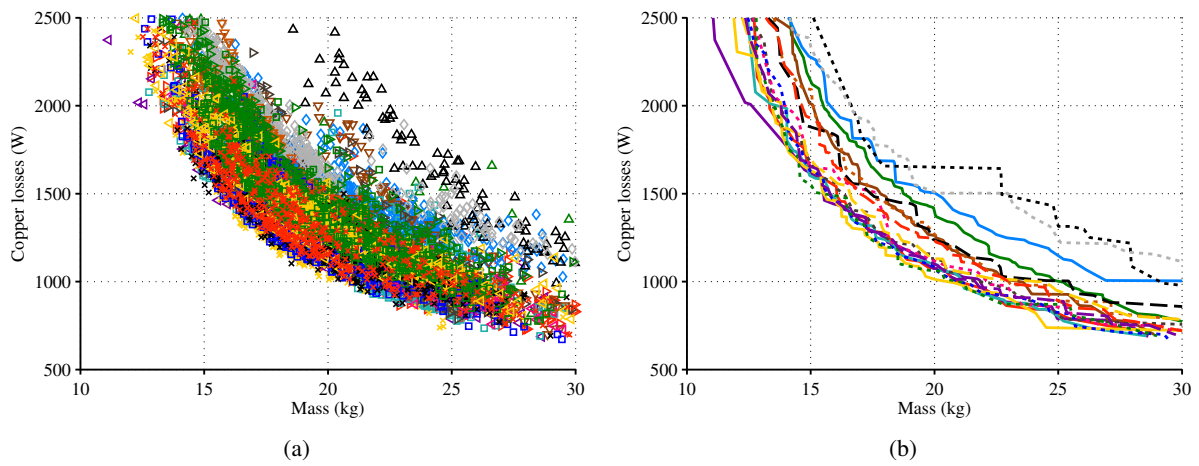


Figure 9: Copper losses at nominal torque

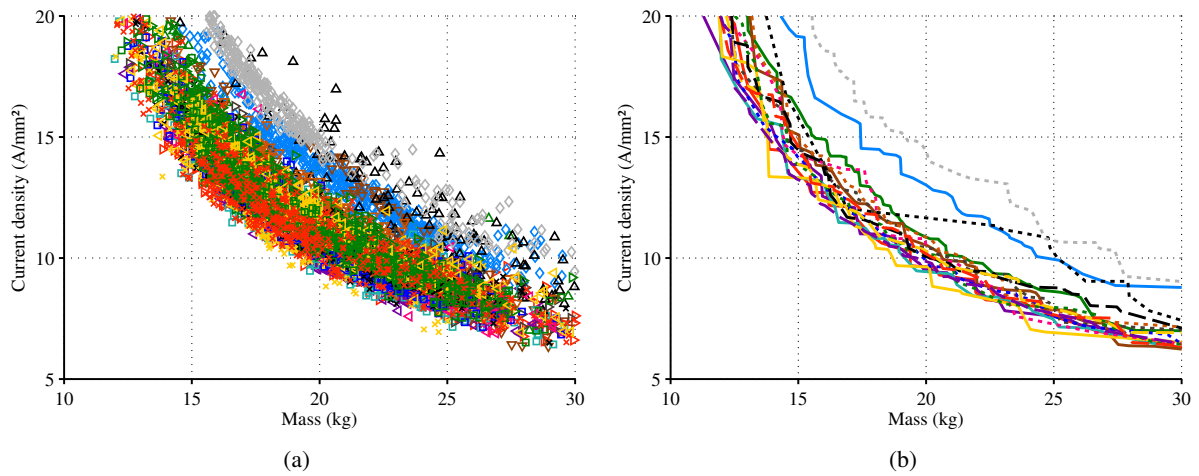


Figure 10: Current density at nominal torque

Table 6 shows the results of the filter operation, sorted for minimum mass. Included are the initial number of designs on the Pareto front; fraction of designs meeting the criteria individually and the intersection of those; and the mass of the lightest motor in the intersection. High pole count motors perform better: the five lightest motors have 48 or 50 poles. The DR motors have the lowest mass, followed by the IR and OR motors. It should be pointed out that the thermal model used here gives only a rough estimate of the temperature and may be biased differently between the three topologies.

Table 5: Filter criteria

| Filter | Description                                 | Lower | Upper: |
|--------|---|-------|--------|
| 1      | Efficiency (%)                              | 95    |        |
| 2      | Max. estimated winding temp. rise (°C)      |       | 120    |
| 3      | Magnet fraction below 0.35 T, 400 Nm (%)    |       | 10     |
| 4      | Extra current due to saturation, 400 Nm (%) |       | 3      |
| 5      | Max B in teeth, Op. 2 (T)                   |       | 1.4    |
| 6      | Max B in yoke, Op. 2 (T)                    |       | 1.4    |
| 7      | Phase inductance (pu)                       | 0.15  | 0.4    |

Table 6: Filter outcome, sorted for minimum mass

|             | Initial | Flt1<br>% | Flt2<br>% | Flt3<br>% | Flt4<br>% | Flt5<br>% | Flt6<br>% | Flt7<br>% | Intersection<br>% | Min. mass<br>kg |
|-------------|---------|-----------|-----------|-----------|-----------|-----------|-----------|-----------|-------------------|-----------------|
| DR 60/50    | 387     | 97        | 65        | 96        | 98        | 62        | 100       | 84        | 2.1               | 16.8            |
| DR 54/48    | 503     | 97        | 57        | 76        | 98        | 42        | 100       | 84        | 10.5              | 17.5            |
| IR 60/50    | 432     | 98        | 53        | 98        | 95        | 57        | 76        | 95        | 20.1              | 18.0            |
| IR 54/48    | 478     | 96        | 46        | 91        | 89        | 69        | 71        | 88        | 14                | 18.5            |
| OR 60/50    | 261     | 97        | 80        | 72        | 87        | 60        | 79        | 83        | 13.4              | 19.0            |
| DR 48/40    | 467     | 97        | 44        | 86        | 99        | 57        | 100       | 86        | 12                | 19.0            |
| DR 45/40    | 485     | 96        | 46        | 86        | 98        | 55        | 100       | 91        | 12.6              | 19.3            |
| IR 48/40    | 743     | 98        | 38        | 99        | 93        | 67        | 48        | 95        | 0.3               | 20.0            |
| IR 3/2 var. | 454     | 97        | 46        | 98        | 94        | 54        | 56        | 72        | 1.8               | 20.6            |
| IR 45/40    | 505     | 96        | 33        | 97        | 93        | 67        | 68        | 94        | 4.6               | 20.8            |
| OR 54/48    | 453     | 97        | 47        | 47        | 94        | 57        | 89        | 91        | 0.2               | 21.0            |
| OR 45/40    | 453     | 91        | 15        | 84        | 90        | 47        | 80        | 87        | 1.1               | 22.4            |
| IR 36/32    | 497     | 93        | 20        | 96        | 78        | 53        | 74        | 80        | 2.6               | 23.1            |
| OR 48/40    | 421     | 96        | 26        | 80        | 91        | 45        | 65        | 93        | 6.2               | 23.9            |
| IR 36/30    | 390     | 92        | 6         | 97        | 92        | 48        | 64        | 94        | 18.2              | 25.9            |
| OR 36/32    | 461     | 87        | 2         | 78        | 72        | 48        | 84        | 75        | 28                | 26.1            |
| OR 36/30    | 137     | 62        | 35        | 22        | 82        | 53        | 64        | 85        | 70.8              | 27.7            |
| OR 3/2 var. | 363     | 93        | 9         | 94        | 89        | 39        | 38        | 80        | 19.8              | 34.2            |

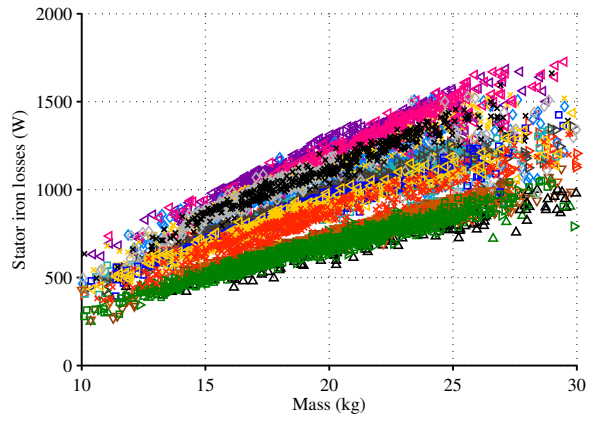
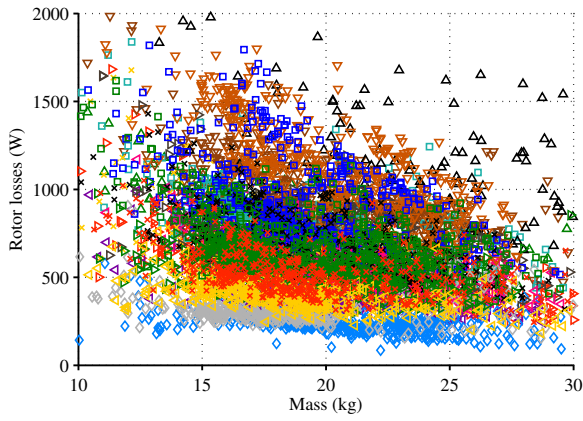
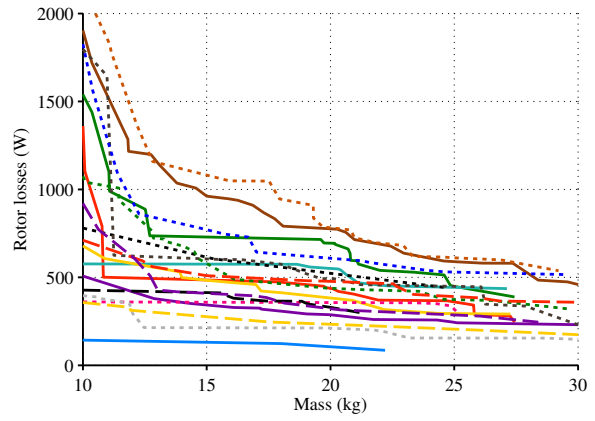


Figure 11: Iron losses

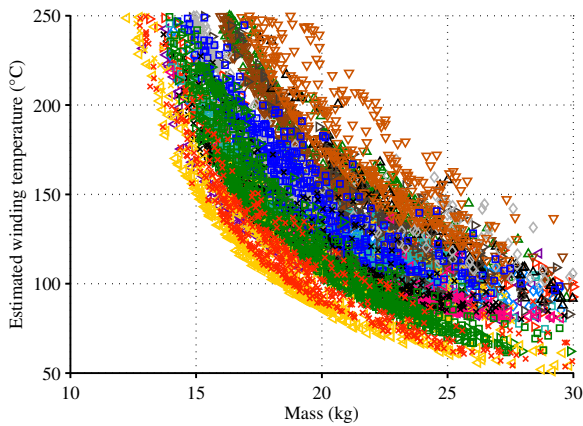


(a)

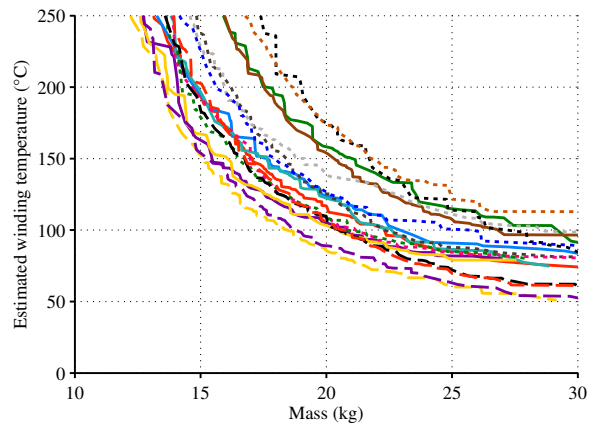


(b)

Figure 12: Rotor eddy-current losses



(a)



(b)

Figure 13: Comparative temperature estimate

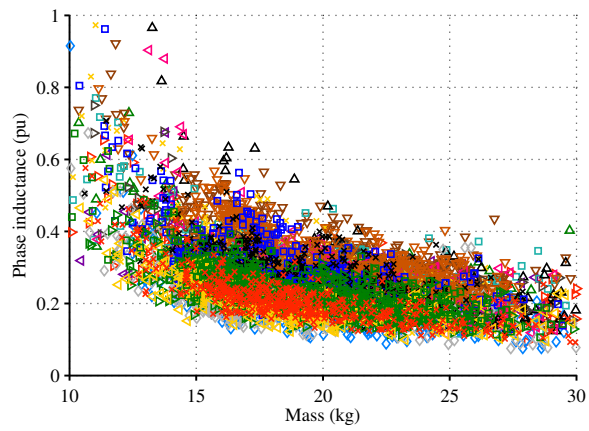


Figure 14: Per-unit phase inductance

## IV. Cooling System Design

Motor cooling system design is introduced and discussed in details. System requirements are reviewed and different motor arrangements and corresponding cooling systems are considered. In order to remain conservative, a motor efficiency of 95% is assumed in the remainder of this section.

### A. System requirements and constraints

Table 7 shows relevant operating conditions for the cooling system while figure 3 references maximum operating temperatures. From a thermal standpoint, climb is the most critical phase because for the following reasons:

- Reduced aircraft (110 knots vs 150 knots in cruise) limits air flow through the system and hence impact the amount of power dissipated.
- Higher power drawn by the motor increases heat dissipation in the system by about 40% compared to cruise conditions.
- Higher free stream air temperatures at lower altitudes at the beginning of the climb phase reduces the temperature gradients in the system, hence decreasing the amount of heat transfer from the motor structure to the air
- Flow angle of attack may negatively impact cooling by reducing the amount of air inlet in the system.

The cooling system must then be sized based on the climb conditions. On the other hand, the cruise phase is critical from a drag point of view, and the cooling drag of the system must therefore be limited. The cooling drag limit in cruise is set not to overcome 2% of the total airplane drag. Cooling drag is defined as the penalty incurred by the cooling system on the aircraft and is obtained by comparison with the clean nacelle performance. It is calculated from an energy perspective as follows:

$$\mathcal{D}_{cooling}[\%] = \frac{(\mathcal{D} + \mathcal{T} - \mathcal{D}_{clean})v}{\dot{E}_{tot}} \quad (1)$$

where  $\mathcal{D}$  and  $\mathcal{D}_{clean}$  represent the drag on the nacelle with and without the cooling system respectively,  $\mathcal{T}$  the torque on the nacelle,  $v$  is the aircraft speed and  $\dot{E}_{tot}$  is the total power drawn by the motors. With electric motors, it is essential that critical components remain under temperature control at all times. Copper wires insulation are particularly sensitive and constitute the first point of failure for a motor under thermal strain. In practice, the maximum operating temperature of the system is set to 120°C.

Power dissipated in the system is another aspect to be considered. While motor efficiency may be as high as 96 – 97%, a conservative assumption of 5% power dissipated is used throughout the cooling analysis. While some of the power gets dissipated in the magnets, most of the heat is generated through the coils and must be dissipated there.

Table 7: Operating Conditions and Design Objectives. \* A free stream of 35°C has been used during simulations. Additional runs are performed at various temperatures for the selected design only.

| Constraint          | Unit  | Max. Value   |
|---------------------|-------|--------------|
| Cruise Drag         | %     | 2            |
| Maximum Temperature | °C    | 120          |
| Condition           | Unit  | Sizing Value |
| Flow Temperature*   | C     | 35           |
| Flow Velocity       | knots | 110          |
| Motor Power         | kW    | 60           |
| Power Dissipated    | kW    | 3            |

In the next section, several air cooling concepts for different motor types are presented and compared using Computational Fluid Dynamics.

## B. Concepts presentation

Throughout the course of the project, different motor designs and associated cooling systems have been proposed. Electric motors can be separated into three categories:

- In Runners (IR): motors with rotating parts (i.e. magnets) located on the inside of the stator as shown in figure 4a.
- Out Runners (OR): motors with rotating parts (i.e. magnets) located on the outside of the stator as shown in figure 4b.
- Double Runners (DR): motors with magnets on both sides of the stator as shown in figure 4c.

Examples of IR and DR motors are presented in figures 4d and e. While DR are typically more intricate than IR or OR, they tend to provide better motor efficiency in certain cases and hence were the preferred arrangement in the early days of the SCEPTOR project. Hence, in an effort to respect the chronology of the project, DR designs will be discussed first.

Note that the main source of heat in the motors considered in this project is always in the stator coils.

### 1. Double Rotor Concept

As explained above, double rotor concepts feature two rows of magnets on either side of the stator. As a result, they present several significant challenges, namely structural support, stiffness and limited room for cooling. In particular, due to the tight space above and below the stator, most of the heat must be evacuated through the narrow rotor/stator gap, and fins can only be placed fore and aft of the stator and not above or below like in IR or OR configurations. In order to maximize cooling, the rotor/stator gap must be increased up to a certain sweet spot where the thermal boundary layer gets fully developed at which point further increase of the gap becomes irrelevant. One possible explanation for this phenomenon is that if the gap size is larger than twice that of the thermal boundary layer, then the air flowing in the center of the channel will not participate in the cooling and will be "wasted". Another factor to consider is that motor efficiency tends to decrease with increasing gap size which in turns affects the amount of heat dissipated. Hence, a certain balance must be found in order to satisfy both motor and cooling efficiency goals.

The main strategy for cooling DR configurations consists in forcing as much flow through the rotor/stator gap in order to evacuate as much heat as possible. Fins can also be added fore and aft of the stator although their efficiency tends to be limited as they are not oriented along the flow. This paper introduces two approaches to DR cooling: a direct design shown in figure 15 and an updraft design shown in figure 17.

In the direct design, as shown in figure 15b, air enters through the inlet located radially out of the spinner and progresses through the rotor stator gap before reaching the exhaust. Moreover, in order to increase the effectiveness of the design, a cowl flap is added just aft of the motor. This is represented as a simple opening and can be observed in the CFD results shown in figure 16. Figure 16a shows a maximum component temperature of  $89^{\circ}\text{C}$  in the climb phase with  $35^{\circ}\text{C}$  free stream temperature. This ensures a margin of  $31^{\circ}\text{C}$  with respect to component rated operating temperatures. As shown in figures 16c and 16d, the flow speed in the  $2\text{mm}$  rotor stator gap reaches about  $40\text{m/s}$ .

The updraft design makes use of the low pressure zone on the top of the lip of the nacelle to provide additional suction and hence increase the mass flow rate through the rotor stator gap. As shown in figure 17c, air enters through the lower inlet and slows down as channel area increases. Upon reaching the back wall, the air is pumped radially out via a blade/vane combination which further builds pressure on the aft face of the stator. Note that the aft stator fins act as both cooling devices and compressor vanes. The air then flows through the rotor stator gap before exiting through the upper lip. Figure 18 presents some CFD results for the updraft design. Under climb conditions at  $35^{\circ}\text{C}$ , the maximum temperature in the system reaches about  $100^{\circ}\text{C}$  as shown in figure 18a. While  $20^{\circ}\text{C}$  under the operating limit, this temperature is noticeably higher than for the direct design. However, the updraft configuration has the advantage of not requiring the addition of a cowl flap which is advantageous in terms of minimizing the number of moving parts. Figures 18b, 18c and 18d showcase the air path and highlight the diffusion process at the inlet of the system, the pressure rise through the compressor and the suction effect of the low pressure zone on the nacelle outer surface.

Double runner motors with high power densities are challenging to design and cool due to stringent geometrical constraints. From a cooling standpoint, the limited surface area available for convection forces the use of intricate designs using cooling cowls or updraft concepts as well as extensive and oddly placed cooling fins. Appropriately cooled double runners for the current design case would lack simplicity and likely incur extensive manufacturing

costs. In addition, the selected OR design's efficiency is within 1% of the best DR design, hence the impact on heat generated is very small. As a result, single rotor designs are favored in the remaining of this paper.

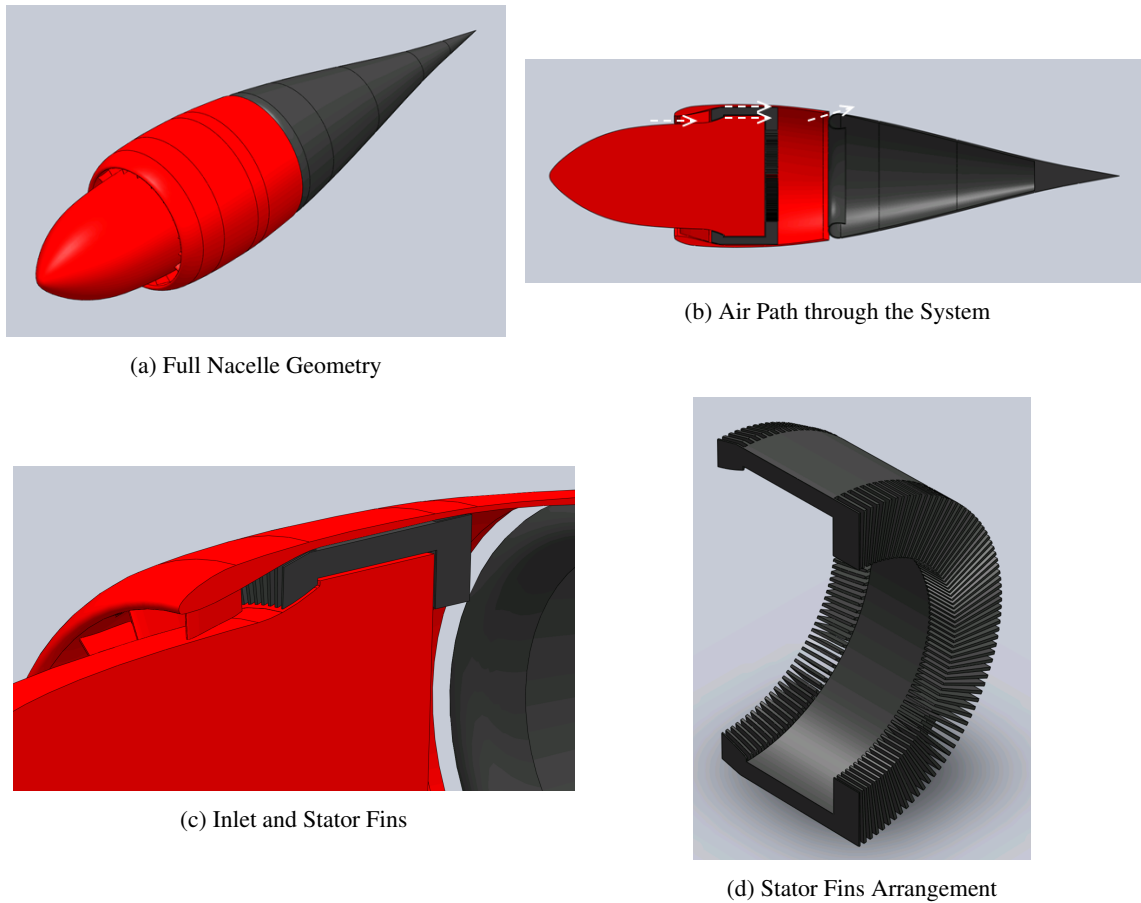


Figure 15: Double Runner with Direct Cooling System and Streamwise Fins. Rotating Parts Displayed in Red

## 2. In Runner

In runner motor designs feature a single row of magnets located on the inner side of the stator as shown in figure 4d. Single rotor designs have several advantages over double rotor motors. Since magnets are only running on one side of the stator, the other side is available for cooling system and structural design. In particular, using fins becomes increasingly practical. Structurally, this allows for a simpler and lighter design. In the case of in runners, one major structural issue arises nonetheless: because the magnets are attached to the outer side of the rotor, the centrifugal force tends to drive them radially outwards towards the stator. Hence, a retaining mechanism must be added. Typically, kevlar or carbon wires are wrapped around the magnets assembly to provide the retaining force. However, one risk is for the wires to come loose and to start rubbing against the stator inner radius, hence further loosening them. Eventually, the magnets may detach and cause failure of the system. In addition, the retaining system acts as an insulating blanket which impedes the cooling of the magnets. Hence, appropriate design of the retaining system is critical and creates additional complexity.

Figure 19 presents the proposed IR design for SCEPTOR. Here, the heat generated in the coils is dissipated by the outer air through the skin. While fins could be added to the outer skin for increased cooling, they would also cause an increase in drag. As shown in figure 19c, the rotor is also fitted with blades to help with air compression. In addition, as shown in figures 19c, 19d, 19e and 19f, the full stator geometry has been included in the CFD model for improved fidelity.

Figure 20 shows CFD results for the proposed IR concept. In particular, it is interesting to note that a significant amount of heat is evacuated through the skin of the nacelle just aft of the motor. The peak temperature for this design is  $74^{\circ}C$  which is  $46^{\circ}C$  under the maximum operating temperature.

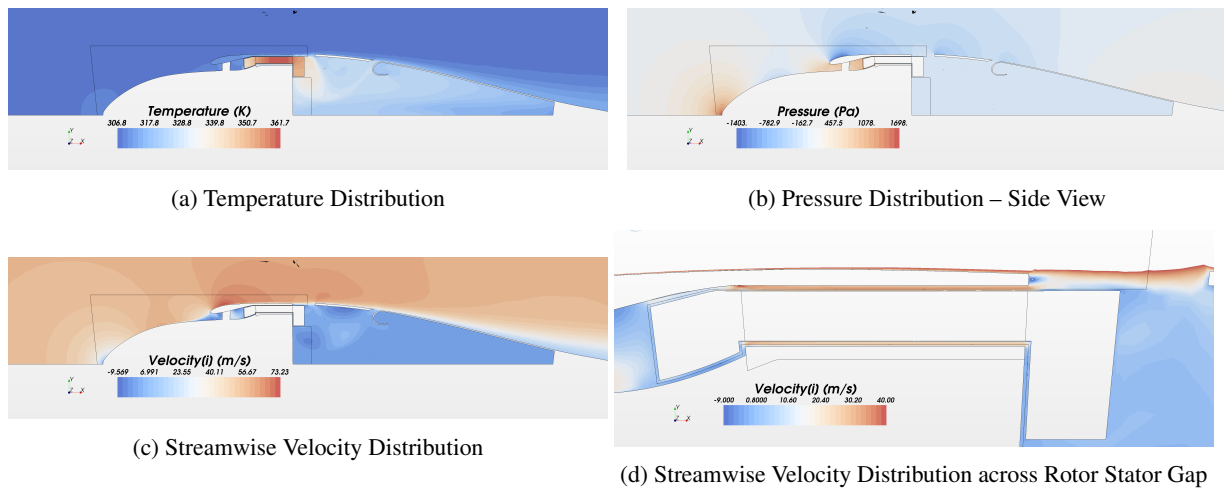


Figure 16: CFD Results – Double Runner with Direct Cooling System – Climb Phase

While structurally simpler than double rotor designs, IR motors present some challenges relating to magnets support, as explained earlier. In particular, design of the wrapping system is a complicated process involving considerations such as pretension analysis, thermal expansion effects or buckling of the structure upon assembly. Improperly designed wrapping may cause the wire to come in contact with the stator inner radius and trigger catastrophic failure. Out Runner, while typically slightly less efficient, remove the need for wrapping magnets and hence greatly simplify the structural design task.

### 3. Out Runner Concept

The OR concept presented in figure 21 features a rotating spinner and outer nacelle, and a fixed inner section housing both the stator and the cooling fins. With magnets located on the inner side of the outer nacelle structure, this design alleviates the need for additional magnet wrapping since the nacelle structure opposes the centrifugal force and retains the magnets. This design makes extensive use of 264 fins to provide cooling for the stator. Fins are designed to maximize face area while achieving high efficiency at around 95% thanks to a low aspect ratio.

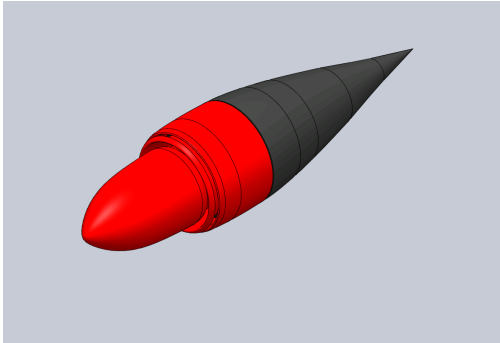
Results presented in figure 22 show a maximum temperature of  $82^{\circ}C$  in climb or  $38^{\circ}C$  under the operating limit of the motor. Note the slightly modified aft nacelle geometry which leads to better flow behavior on the trailing edge and in turns reduces drag. However, despite this modification, the drag remains higher than for the IR design which can be explained by the presence of the fins. The flow speed in between the fins reaches about  $20m/s$  as seen in figures 22c and 22f. Finally, figure 22e shows a high temperature gradient in the fins which means that the problem is convection dominated. It could be beneficial to swap the aluminum used in the fins for a more heat conductive material.

## C. Concepts Comparison

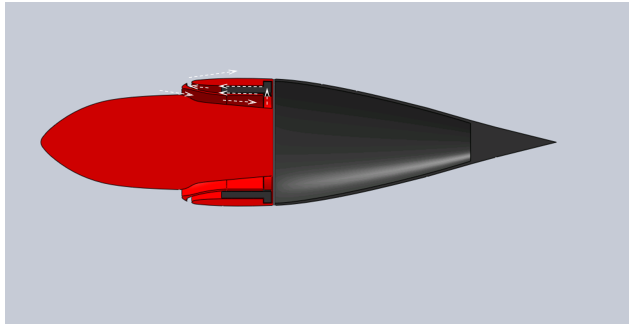
Table 8 compares performances of the different designs presented in section B in terms of temperature and drag performance. The drag performance is more relevant in cruise as the aircraft will spend most of its flight time in this condition. On the other hand, temperature considerations are critical during the climb phase where motor components may overheat. As explained earlier, the cooling drag is calculated by considering the additional drag imparted on the airplane by the cooling system as computed according to equation 1. Note that here, the total power drawn by the motors,  $60kW$  in climb and  $43kW$  in cruise.

Results show that both IR and OR designs achieve better cooling than DR configurations, both in terms of operating temperature and drag. Double Runner designs were first considered because they could provide better motor efficiency. However, the latest IR and OR designs come very close to DR in terms of efficiency and hence the benefits of the latest were limited. Moreover, DR configurations are more intricate from a structural standpoint. As a result, these designs were quickly discarded.

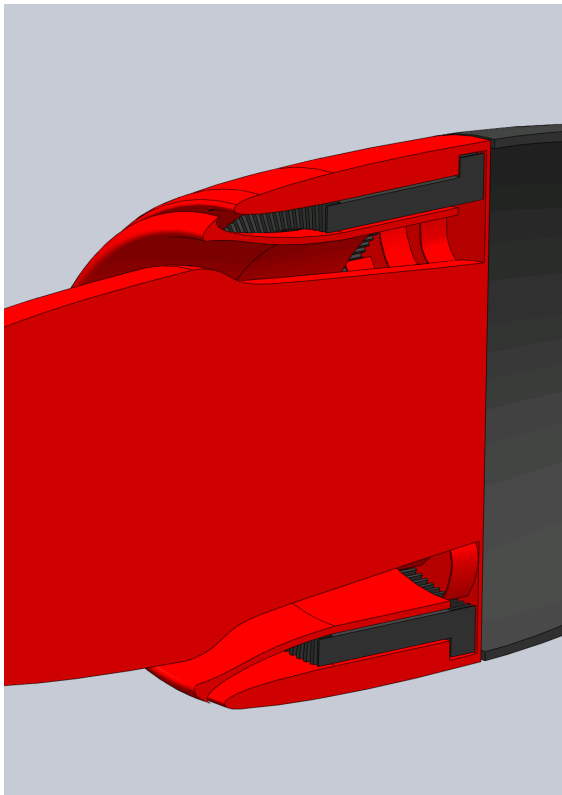
As seen in table 8, IR designs achieve lower operating temperatures and cruise drag than OR designs. This is due to the fact that with the stator placed on the outside, IR designs fully leverage the outer nacelle surface for additional



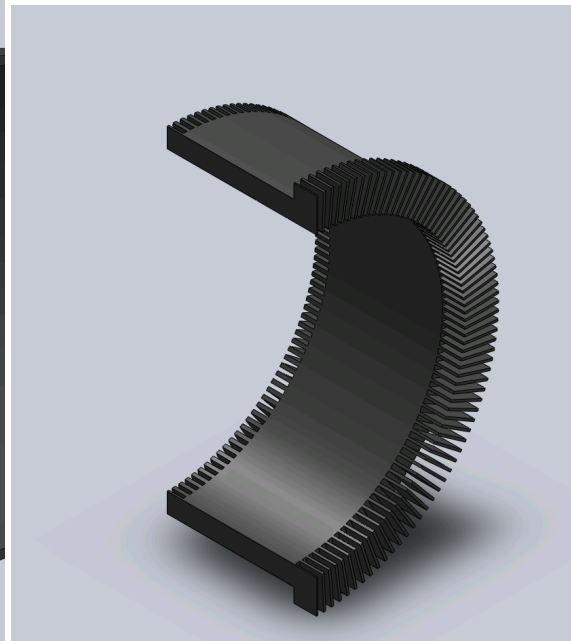
(a) Full Nacelle Geometry



(b) Air Path through the System



(c) Inlet and Stator Fins



(d) Stator Fins Arrangement

Figure 17: Double Runner with Updraft Cooling System

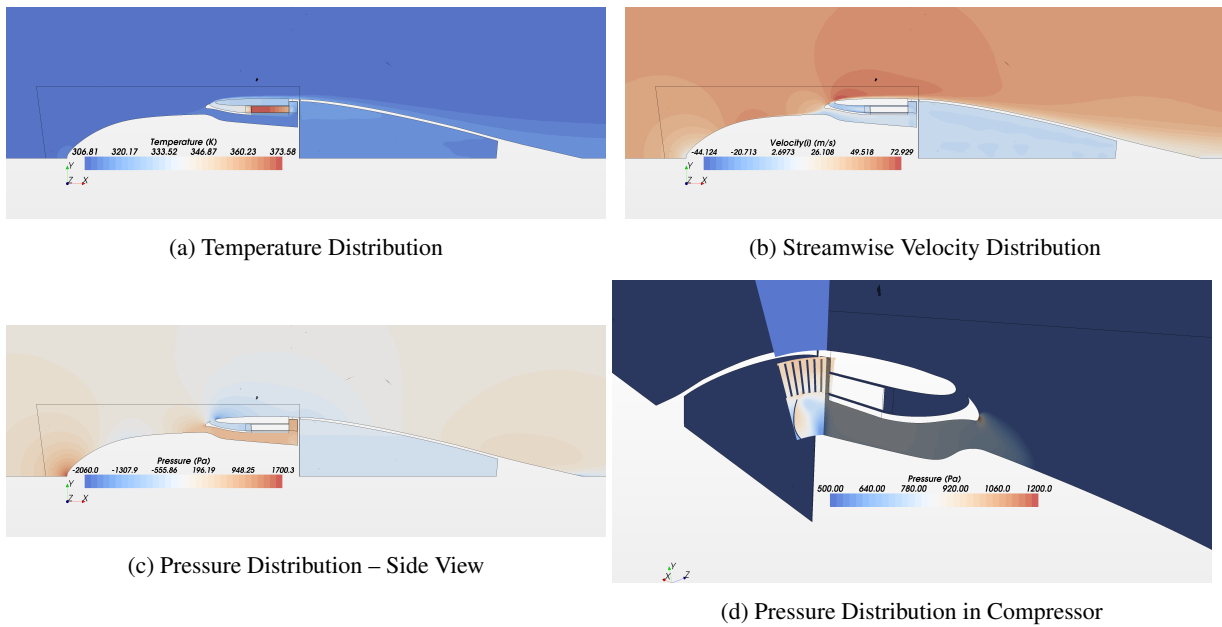
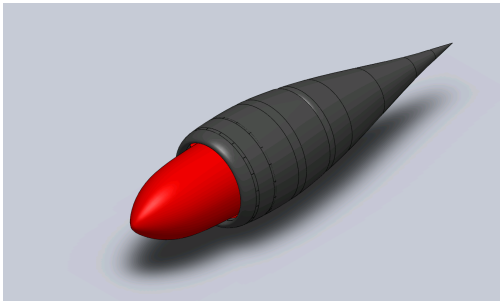


Figure 18: CFD Results – Double Runner with Updraft Cooling System – Climb Phase

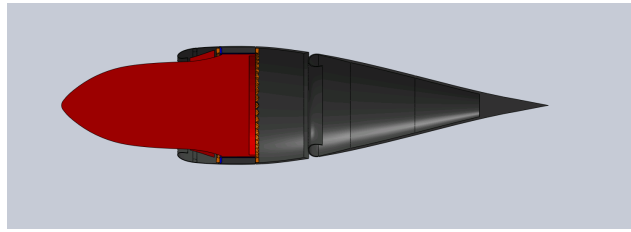
cooling at no extra drag cost. On the other hand, the proposed OR system has to resort to additional fins to provide sufficient cooling, which reduces the drag performance of the system. From a cooling standpoint, the IR design is the preferred configuration. However, IR designs come with several structural drawbacks:

- The magnets must be retained to prevent them from escaping radially out due to the centrifugal force. This is typically done by wrapping them in Kevlar or Carbon wires. However, one risk is for the wires to come loose and to start rubbing against the stator inner radius, hence further loosening them. Eventually, the magnets may detach and cause failure of the system. In addition, the retaining system acts as an insulating blanket which impedes the cooling of the magnets. Hence, appropriate design of the retaining system is critical.
- In terms of structural support, IR designs create additional issues. In particular, supporting the propeller spinning in front of the nacelle is difficult to achieve with the proposed IR design. This is because the support structure and the bearings would have to be placed aft of the motor and hence would be subject to a high moment. As a result, the support structure would have to be quite substantial (and hence heavy) to achieve the desired performances. On the other hand, the OR design allows for support structures to be placed both fore and aft of the motor which is desirable from a structural perspective.

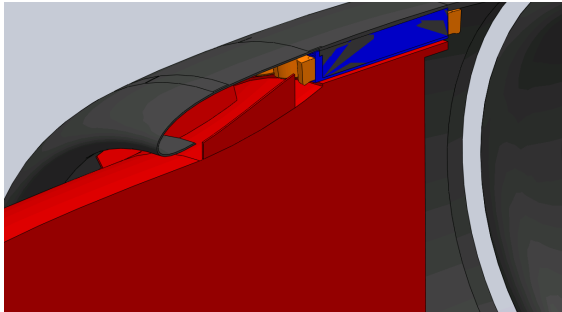
While not being the best thermal design, the Out Runner configuration provides very good thermal performance with a predicted operating margin of  $38^{\circ}C$  and a cruise drag of 1.6%. In addition, it provides several structural advantages, and hence represents the best compromise between motor performance, cooling and structural design. As a result, the Out Runner configuration presented in figure 21 is selected for the SCEPTOR tip nacelle.



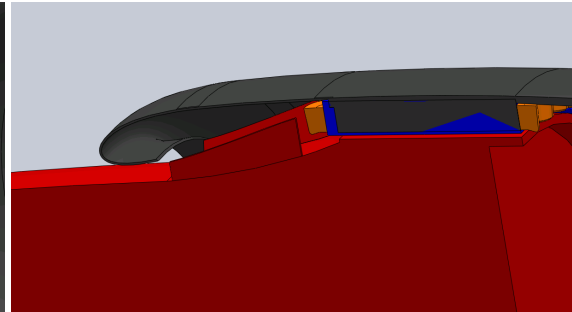
(a) Full Nacelle Geometry



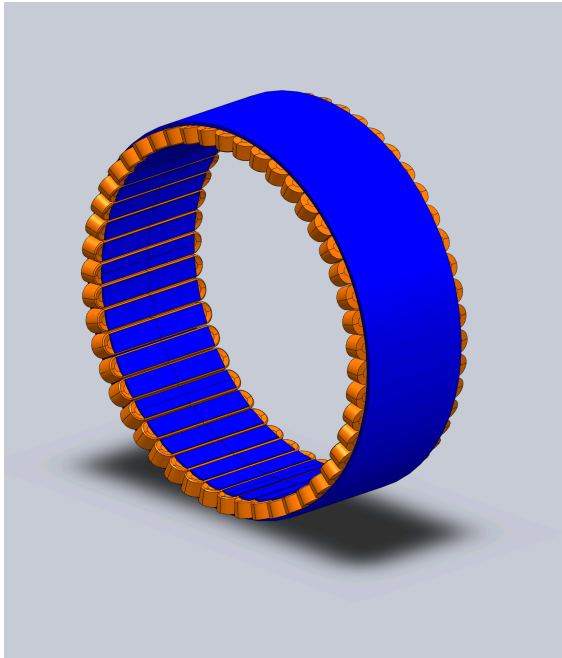
(b) Side View



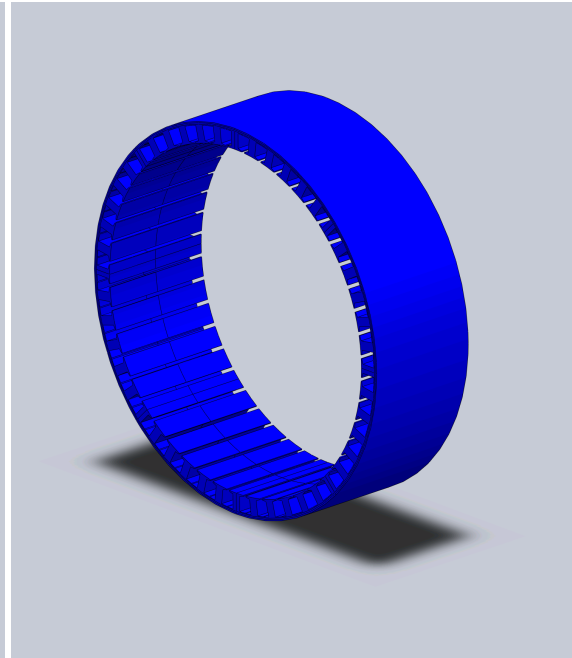
(c) Inlet and Rotor Fins



(d) Inlet Lip and Rotor Fins



(e) Stator Fins Arrangement



(f) Stator Fins Arrangement

Figure 19: In Runner with Direct Cooling System

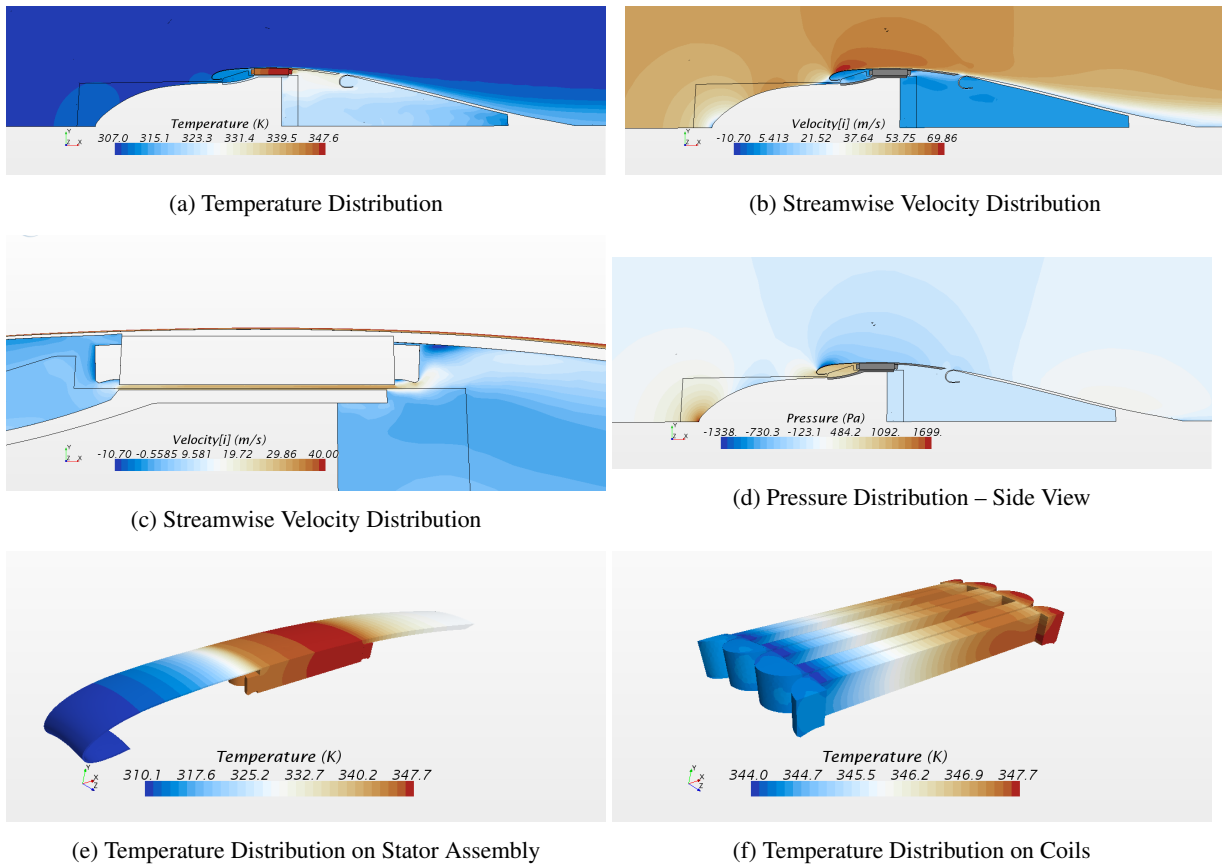
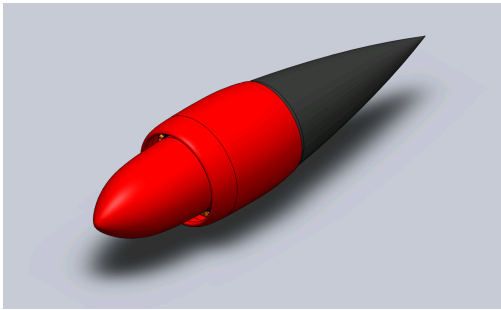


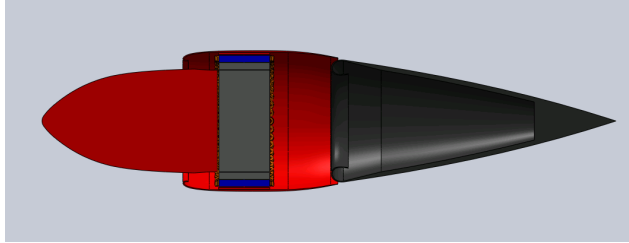
Figure 20: CFD Results – In Runner – Climb Phase

Table 8: Design Performance Summary. Drag in  $W$  if obtained as  $[Drag[N] \times Speed[m/s]]$ . Torque in  $[W]$  is obtained as  $[T[N] \times Rot.Speed[rad/s]]$ .

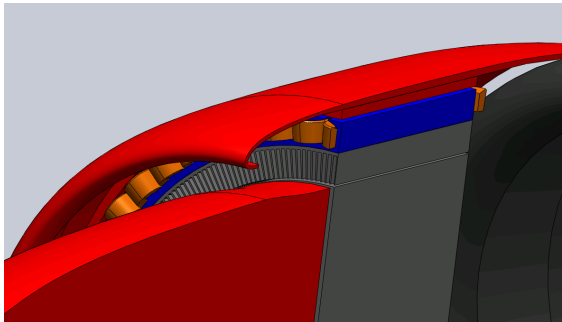
|        |                  | Clean Nacelle | DR Direct | DR Updraft | IR   | OR   |
|--------|------------------|---------------|-----------|------------|------|------|
| Climb  | Drag [W]         | 864           | 1478      | 1863       | 1275 | 1354 |
|        | Torque [W]       | NA            | 226       | 249        | 134  | 195  |
|        | Max Temp [K]     | NA            | 362       | 376        | 348  | 355  |
|        | Cooling Drag [%] | NA            | .96       | .70        | .56  | .72  |
| Cruise | Drag [W]         | 389           | 1065      | 919        | 610  | 649  |
|        | Torque [W]       | NA            | 247       | 238        | 112  | 172  |
|        | Max Temp [K]     | NA            | TBD       | 315        | 311  | 295  |
|        | Cooling Drag [%] | NA            | 1.95      | 2.04       | 1.3  | 1.6  |



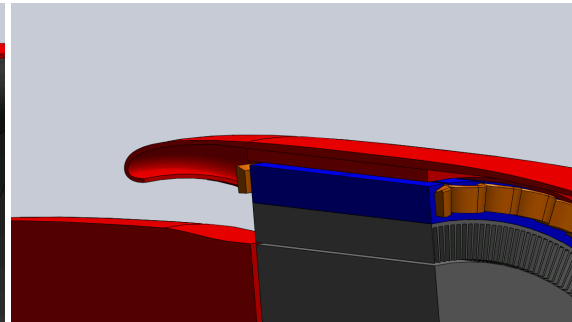
(a) Full Nacelle Geometry



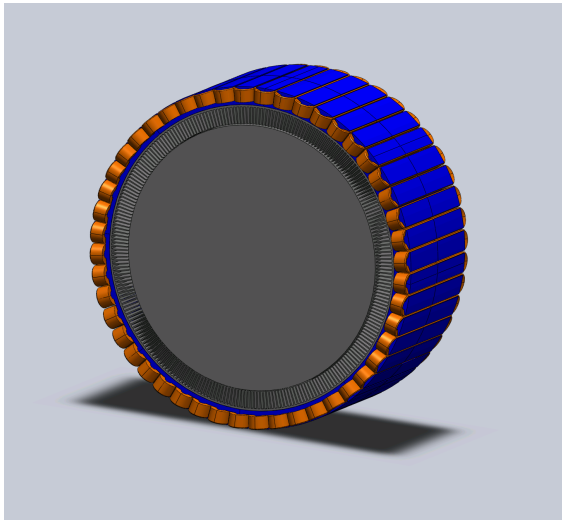
(b) Side View



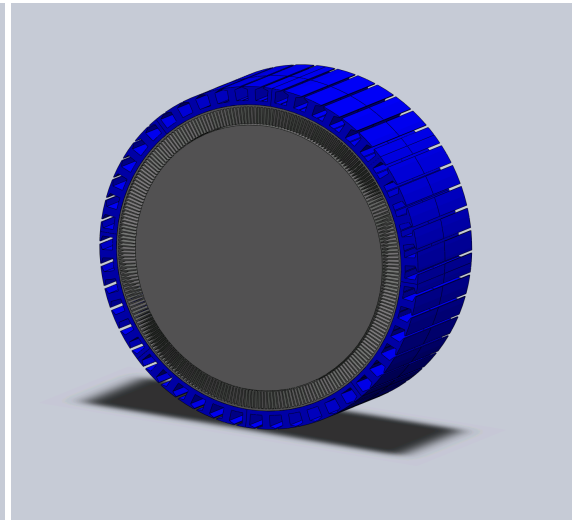
(c) Inlet and Rotor Fins



(d) Inlet Lip and Rotor Fins

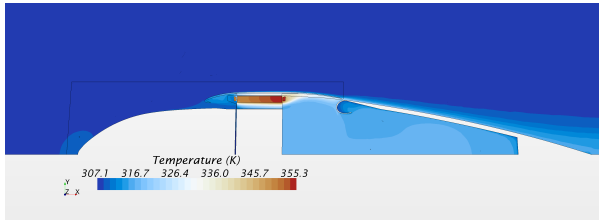


(e) Stator Fins Arrangement

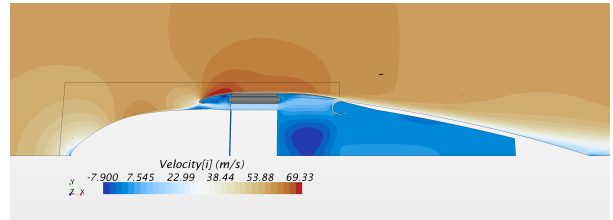


(f) Stator Fins Arrangement

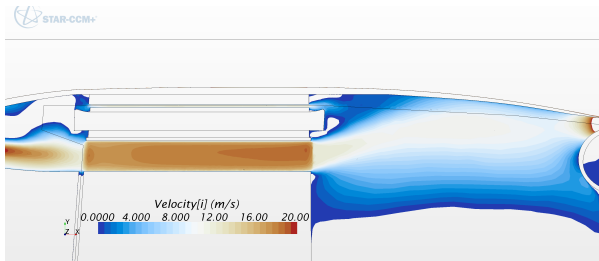
Figure 21: Out Runner with Direct Cooling System



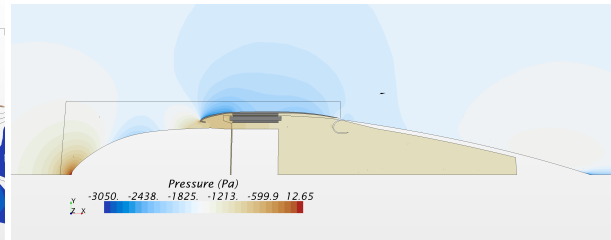
(a) Temperature Distribution



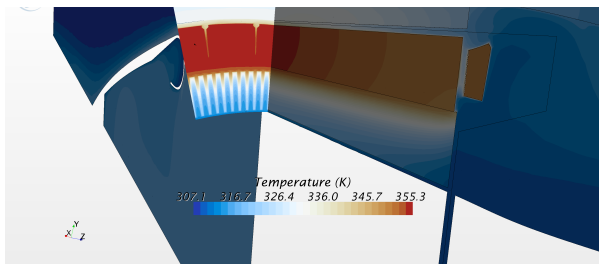
(b) Streamwise Velocity Distribution



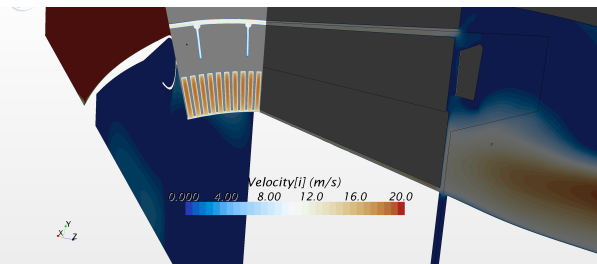
(c) Streamwise Velocity Distribution



(d) Pressure Distribution – Side View



(e) Temperature Distribution on Stator Assembly



(f) Temperature Distribution on Coils

Figure 22: CFD Results – Out Runner – Climb Phase

## V. Overview of Selected Design

### A. Motor

A candidate motor design is selected from the optimization results and serves as input for a more detailed design, which will be described in this section. These results serve as input to the detailed thermal analysis.

The decision for a certain motor topology was not only based on the outcome from the previous section, but also on practical considerations such as mechanical considerations, electrical frequency, and winding considerations. In fact, an IR motor was considered as first candidate, but changed to OR after facing mechanical issues. The selected motor has a 48/40 configuration with an active mass of 22 kg. Table 9 provides the basic properties of this prototype candidate design.

Table 9: Basic motor properties

|                           |  |
|---------------------------|--|
| Active mass               | 22.2 kg  |
| Stack length              | 128 mm   |
| Losses at 320 Nm 2250 RPM | Copper: 1.1 kW DC + 0.2 kW AC<br>Iron: 1.1 kW<br>Rotor: 0.6 kW |
| Inductance                | 40–60 $\mu\text{H}$ /inverter (= 0.2–0.3 pu)                   |
| Nominal phase current     | 115 $A_{\text{rms}}$ /inverter                                 |

#### 1. Torque performance

Figure 23 shows the expected torque versus the motor currents in the  $dq$ -frame. In an ideal SPM motor the torque is independent of the  $d$ -axis current and increases linearly with the  $q$ -axis current. In reality, saturation due to high currents reduces the output torque, which can partially be alleviated with some negative  $d$ -axis current, which is also visible in the plot. In practice this means that the ideal current angle is slightly current dependent. In this motor design, this effect is relatively small, indicating that the magnetic safety margin is large.

#### 2. Efficiency

Figure 24 shows the efficiency versus output torque and speed. The efficiency in the nominal operating point is about 96–96.2%. The point of optimal efficiency lies at a slightly higher speed, caused by using very low loss laminations.

#### 3. Parasitic winding losses

The combination of the slot size, number of turns and nominal electrical frequency of 800 Hz potentially leads to proximity losses in the winding. Those losses can be kept at an acceptable level by using bundles of parallel strands and twisting the bundles in more extreme cases.<sup>6</sup>

Figure 25 shows the estimated proximity losses versus number of parallel strands in the nominal operating point. The losses become acceptable with about 6 or more parallel wires. As an example figure 26 shows a finite element solution of the motor with 8 parallel wires per coil. This shows that the extra losses occur mostly near the slot opening, where most of the slot leakage flux exists. Of the extra losses shown in figure 25, 60% is caused by the PM leakage flux and occurs even without stator currents applied. The prototype motor is wound with 7 strands.

### B. Cooling System

Figure 27 gives an overview of the selected Out Runner design along with all structural details. Figure 27b showcases the support of the spinner/outer nacelle assembly which is accomplished by two bearing fore and aft of the motor. This ensures that the heavy propeller assembly located in the front is always secured. Figure 28 shows the evolution of drag and maximum temperature as the angle of attack of the plane is increased during climb. In particular, it seems like the temperature penalty is relatively small as the angle of attack increases which is critical for the motor to operate. On the other hand, there is a significant drag penalty for increasing the climb angle of attack of the aircraft.

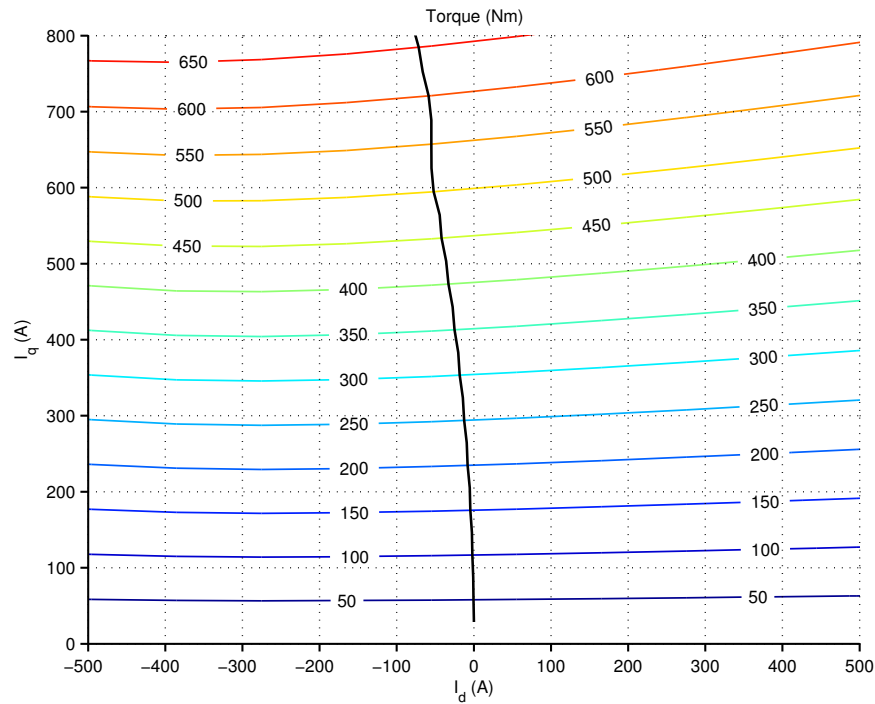


Figure 23: Simulated torque versus  $dq$  currents, with the optimal current trajectory (maximum torque per amp) indicated.

The prototype qualification temperature for the aircraft is set to  $60^{\circ}C$  according to figure 3 while the maximum operating temperature for motor components is  $120^{\circ}C$ . Figure 29 shows the evolution of the motor temperature as free stream air temperature increases. The figure shows a somewhat linear trend in the temperature behavior. However, the rate of increase of motor temperature increases as free stream temperature rises, which can be explained by smaller temperature gradients hence worsening the heat transfer.

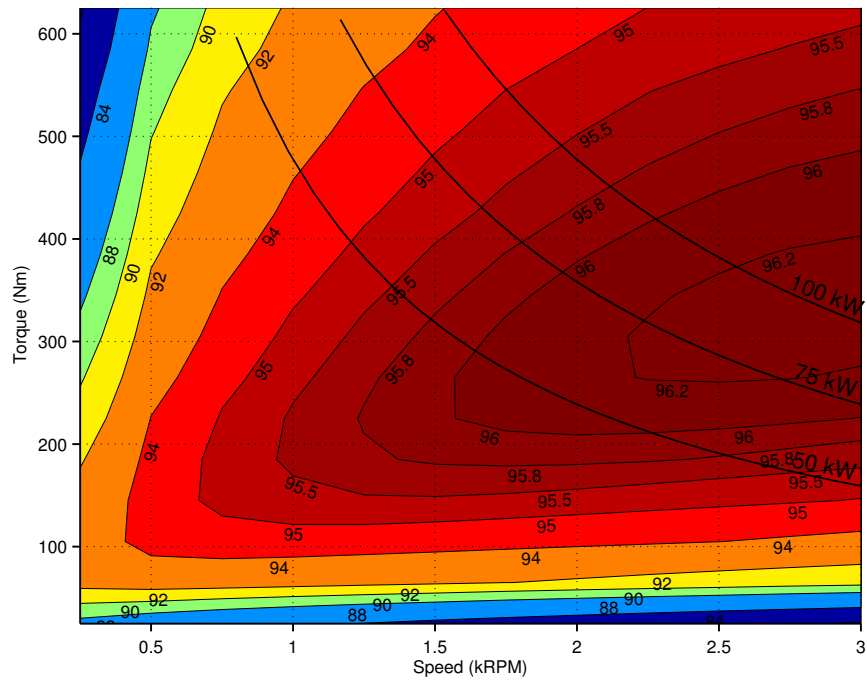


Figure 24: Simulated efficiency versus torque and speed.

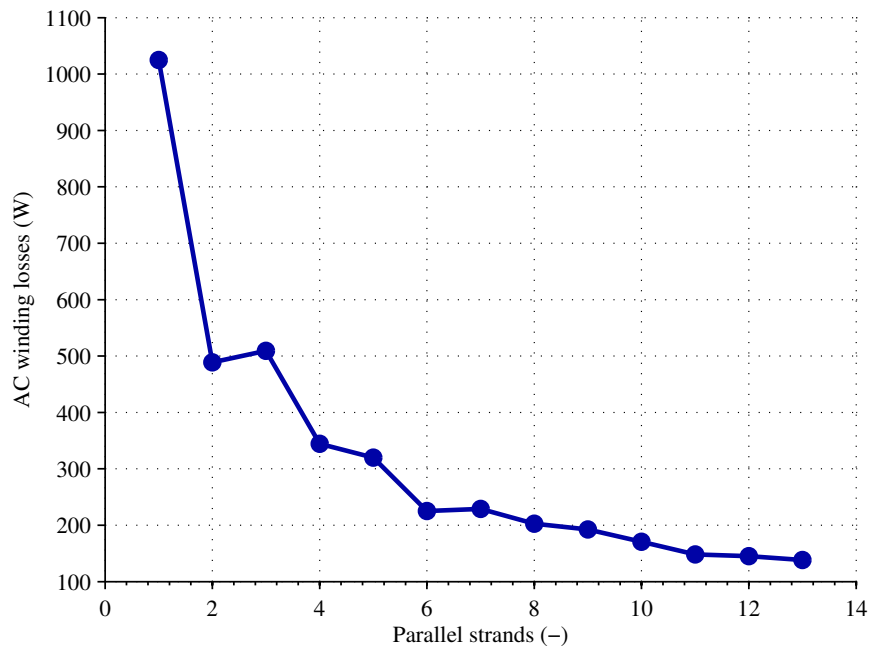


Figure 25: Estimated winding proximity losses versus number of parallel strands.

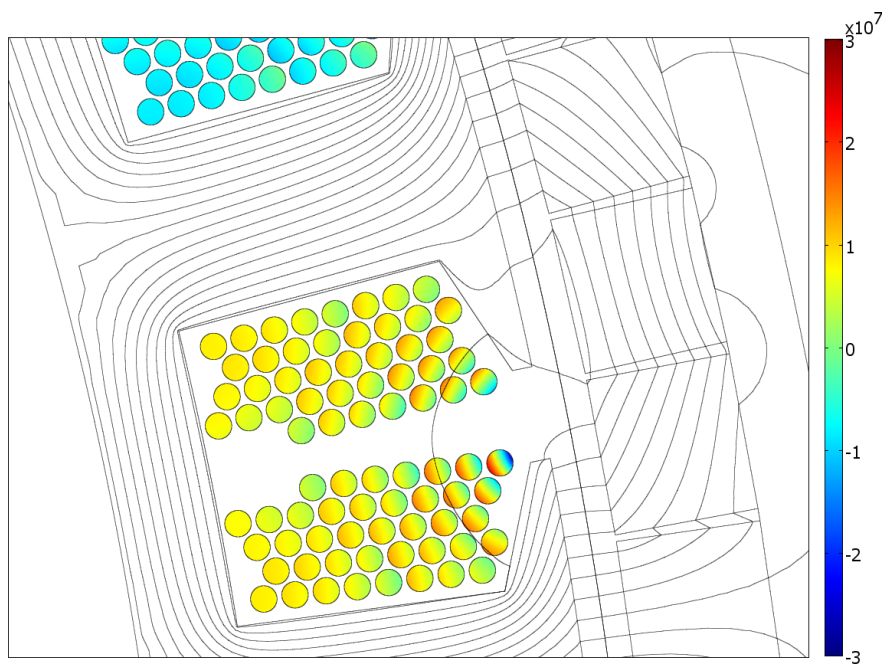
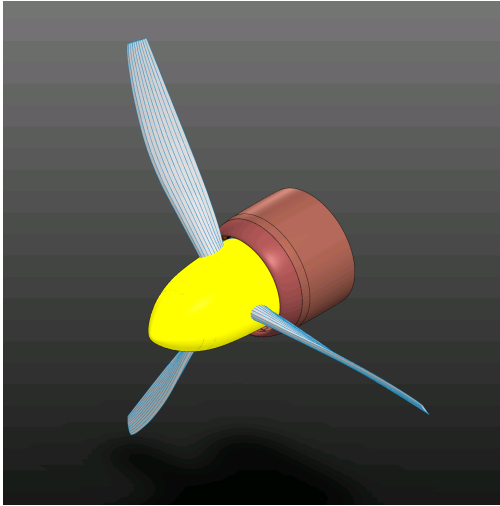
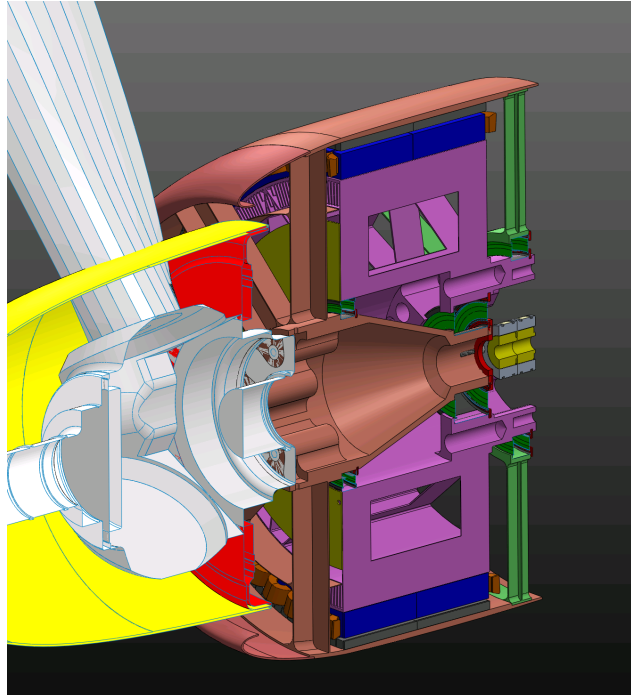


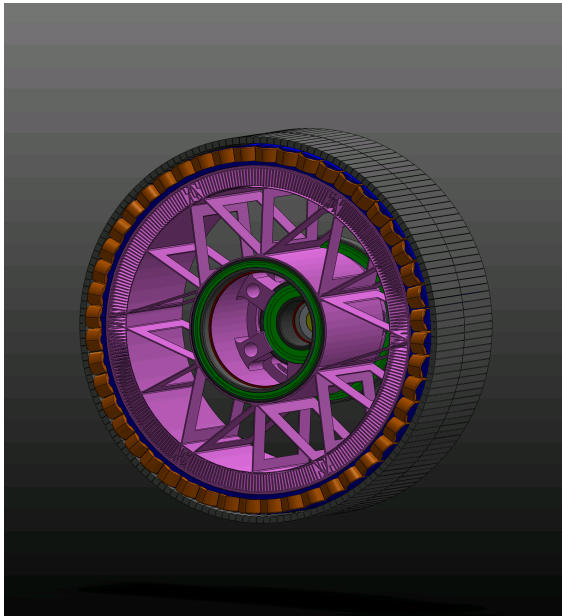
Figure 26: Current density distribution in the motor windings with 40 strands per slot.



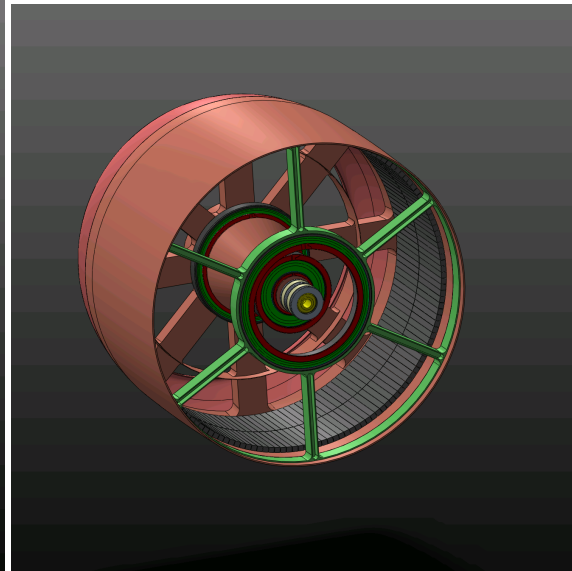
(a) Full Nacelle Geometry



(b) Slice – Full Geometry



(c) Stator



(d) Rotor

Figure 27: Selected Out Runner Design – Preliminary Detailed Design

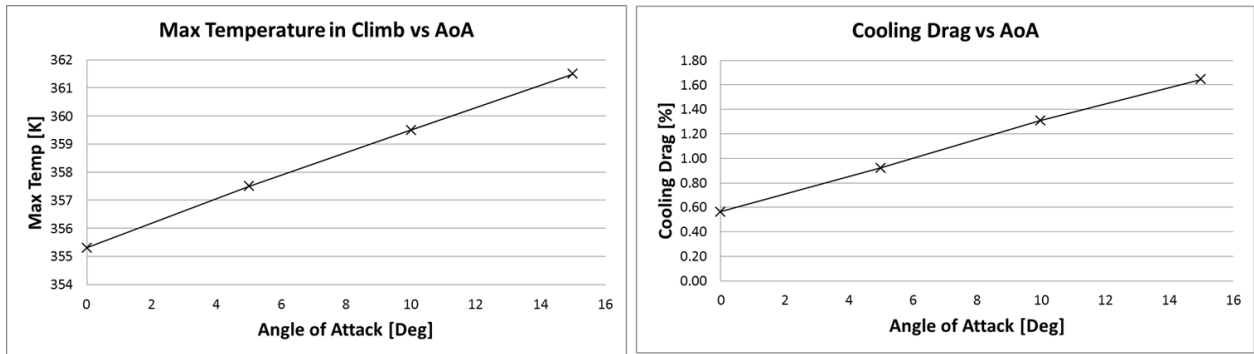


Figure 28: Cooling System Performance vs AoA in Climb.

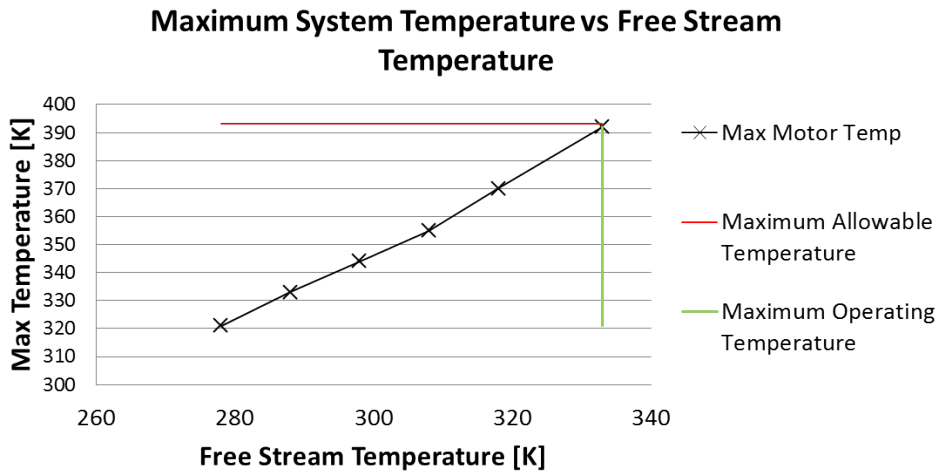


Figure 29: Maximum System Temperature in Various Free Stream Conditions.

## VI. Conclusion

This paper summarizes the design process for the outboard nacelle design of the SCEPTOR demonstrator aircraft. Both motor design and cooling aspects were explored, and major trade offs were presented. In addition to cooling and motor efficiency, a large number of additional parameters were evaluated in the decision process, including mechanical and structural considerations, electrical frequency and coils winding. The selected design features an Out Runner motor with a 48/40 configuration and mass of  $22\text{kg}$ . The cooling system uses direct air cooling for the stator through a fin system. The motor is expected to provide up to  $500\text{Nm}$  of torque at about 96% efficiency. The cooling system is expected to maintain the motor components temperatures under  $120^\circ\text{C}$  at up to  $60^\circ\text{C}$  outside temperature. During climb, the motor temperature is expected to reach  $82^\circ\text{C}$  on a hot day. The motor and nacelle are currently in the manufacturing and test phase.

## Acknowledgments

The authors would like to acknowledge the support of the SCEPTOR cooling IPT team for their help throughout this project. In addition, the authors would like to thank Scott MacAfee and Evan Wu for their contribution to the detailed design of the motor.

## References

- <sup>1</sup>Stoll, A. M., Bevirt, J., Moore, M. D., Fredericks, W. J., and Borer, N. K., *Drag Reduction Through Distributed Electric Propulsion*, 14th AIAA Aviation Technology, Integration, and Operations Conference, American Institute of Aeronautics and Astronautics, June 2014.
- <sup>2</sup>Stoll, A. M. *Comparison of CFD and Experimental Results of the LEAPTech Distributed Electric Propulsion Blown Wing*, 14th AIAA Aviation Technology, Integration, and Operations Conference, American Institute of Aeronautics and Astronautics, June 2015.
- <sup>3</sup>Reddy, P. B.; El-Refaie, A. M.; Huh, K.-K.; Tangudu, J. K. and Jahns, T. M., "Comparison of Interior and Surface PM Machines Equipped With Fractional-Slot Concentrated Windings for Hybrid Traction Applications," IEEE Trans. Energy Conversion, 2012, vol. 27, pp. 593–602.
- <sup>4</sup>Binder, A. and Schneider, T. and Klohr, M., "Fixation of buried and surface-mounted magnets in high-speed permanent-magnet synchronous machines," IEEE Trans. Ind. Appl., 2006, vol. 42, pp. 1031–1037.
- <sup>5</sup>Van der Geest, M.; Polinder, H.; Ferreira, J. A. and Zeilstra, D., "Design and Testing of a High-Speed Aerospace Permanent Magnet Starter/Generator," 3<sup>rd</sup> Int. Conf. Electrical Systems Aircraft, Railway, Ship propulsion and Road Vehicles (ESARS), 2015.
- <sup>6</sup>Van der Geest, M.; Polinder, H.; Ferreira, J. and Zeilstra, D., "Current sharing analysis of parallel strands in low voltage high speed machines," IEEE Trans. Ind. Electronics, 2014, vol. 61, pp. 3064–3070.